

## Angular momentum and moment of total enthalpy integral equations for high-speed boundary layers

Armin Kianfar <sup>\*</sup>

*Department of Mechanical & Aerospace Engineering, University of California, Irvine, California 92617, USA*

Mario Di Renzo 

*Department of Engineering for Innovation, University of Salento, Lecce, Italy  
and Center for Turbulence Research, Stanford University, Stanford, California, USA*

Christopher Williams  and Ahmed Elnahas 

*Center for Turbulence Research, Stanford University, Stanford, California 94305, USA*

Perry L. Johnson 

*Department of Mechanical & Aerospace Engineering, University of California, Irvine, California 92617, USA*



(Received 28 February 2023; accepted 5 April 2023; published 5 May 2023)

The enhancement of skin-friction drag and surface heat flux by the transition to turbulence is a crucial physical phenomenon for the design of high-speed vehicles. An interpretable mapping of how various flow phenomena such as turbulence and the streamwise growth of the boundary layer (BL) thickness influence these key surface quantities is desirable for advancing our understanding of fundamental flow physics, as well as informing engineering design analysis. To accomplish such a mapping, an angular momentum integral (AMI) equation, originally derived for incompressible flows by Elnahas and Johnson [*J. Fluid Mech.* **940**, A36 (2022)], is here introduced for compressible turbulent BL flows of a calorically perfect gas. By isolating the laminar BL friction at the same Reynolds number, the AMI equation obtains a straightforward interpretation for skin-friction alteration by other flow phenomena relative to an equivalent laminar BL. Similarly, a moment of total enthalpy integral (MTEI) equation is proposed to quantitatively map the effects of turbulence and other physical flow phenomena to the Stanton number relative to an equivalent laminar BL. Direct numerical simulations (DNSs) of zero pressure gradient isothermal flat plate BLs up to edge Mach number of 7 are used to demonstrate the utility of the AMI and MTEI equations. The DNS cases span a variety of wall-temperature boundary conditions ranging from nominally adiabatic to strongly cooled walls. The derivation of the AMI equation itself suggests the use of shear stress-weighted average viscosity, which collapses the relative influence of turbulence on compressible BL skin friction over the wide range of edge Mach numbers and temperature boundary conditions considered. The AMI results quantify how the variation of mean density inside a turbulent BL impacts the ability of correlated velocity fluctuations to transport momentum and enhance the skin friction coefficient relative to the equivalent laminar BL. From an alternative viewpoint, the results demonstrate how the effect of compressibility on laminar BLs can be used to gain insight into turbulent BLs. The MTEI results similarly demonstrate how the mean density alters the impact of turbulence on the transport of total enthalpy and Stanton number. In doing so, the MTEI results highlight the relative role of turbulent fluxes of enthalpy and mean kinetic energy on the Stanton number. In light of these results, the AMI and MTEI

---

<sup>\*</sup>Corresponding author: akianfar@uci.edu

equations provide a quantitative perspective on the fundamental physics of skin friction and surface heat flux in high-speed BLs, which may prove useful for evaluating flow control schemes and complementing existing analysis tools.

DOI: [10.1103/PhysRevFluids.8.054603](https://doi.org/10.1103/PhysRevFluids.8.054603)

## I. INTRODUCTION

The transition to turbulence in boundary layers (BLs) is accompanied by a significant jump in skin friction and surface heat transfer. Depending on the application, this may be beneficial or deleterious. A fully turbulent wall-bounded flow is characterized by coherent structures with a wide range of length scales and differing wall-normal distances [1]. These turbulent structures increase wall-normal momentum transport via Reynolds shear stress, generating higher wall shear stress and skin friction drag specifically in streamlined bodies. For high-speed vehicles, however, drag is often less crucial than tremendous surface heat flux. Supersonic and hypersonic flows are energetic and create high-temperature regions that directly diminish the aerodynamic performance and make the flow control schemes less efficient [2]. Elevated heat fluxes caused by transition to turbulence pose an existential threat to high-speed vehicles and a persistent barrier to the development of hypersonic flight [3]. Therefore, understanding the turbulent structures and physics responsible for the enhancement of surface shear stress and heat transfer is of paramount importance for aerodynamics applications.

Central to our present understanding is the hypothesis of Morkovin [4]. He postulated that density and enthalpy fluctuations do not significantly impact the turbulent time and length scales, which is often true for BLs below the hypersonic regime in which the turbulent Mach number is much lower than unity. Later, Spina and Smits [5] experimentally showed evidence that the influence of compressibility on turbulent large-scale organized structures is relatively minor for (relatively low Mach number) supersonic BLs. As such, our understanding of turbulence in compressible BLs often borrows heavily from our (comparatively more mature) understanding of incompressible turbulent BLs. Fully turbulent BLs are commonly partitioned into inner, outer, and overlap layers. As summarized below, for incompressible BLs, each region is characterized by its flow patterns and coherent motions.

Within the inner layer—in which the viscous effect is non-negligible—streamwise streaks and streamwise-oriented vortical structures are prevalent [6,7]. These streaks and vortices can self-sustain independent of the presence of large-scale motions (LSMs) in the outer region [8,9]. For incompressible flows at high Reynolds numbers, the logarithmic overlap region is associated with a hierarchy of self-similar attached eddies [10], which forms the foundation of the attached-eddy model [11]. In the inner layer and overlap region, significant effort has been expended to identify an effective transformation that collapses compressible BL profiles onto their incompressible counterparts [12]. In particular, such transformations seek to reproduce the logarithmic dependence of mean velocity on wall distance in an overlap layer. For many years, the van Driest transformation [13], which is based on the mean density profile, was considered the most generally successful of these compressible BL transformations. Using a semilocal scaling based on viscosity, an improved collapse in the velocity RMS profiles was demonstrated [14,15]. More recent years have seen a re-invigoration of such efforts, including a viscosity weighted transformation based on turbulence equilibrium proposed by Zhang *et al.* [16], as well as the transformation of Trettel and Larson [17], who included the mean viscosity profile in their systematic approach to the velocity transformation. Following this, a number of other transformations have been proposed in recent years, e.g., Refs. [18–20]. At present, it does not appear that a consensus has formed regarding the relative performance of these more recent transformations, though it remains an active area of research.

The outer layer is populated by LSMs with a streamwise size comparable to and even exceeding the boundary thickness [21]. In addition, elongated coherent structures of streamwise velocity above the logarithmic region are known to form superstructures or very-large-scale motions (VLSMs) [22]. They often extend over 20 times the BL thickness and affect the inner layer [23]. These superstructures were observed in a similar manner as large-scale coherent motions for supersonic turbulent BLs [24]. Although the turbulent structures in inner and outer regions are physically different, it was experimentally shown that the maximum of the streamwise turbulent intensity does not scale with inner units [25]. In other words, the inner viscous region depends on the Reynolds number, and therefore on the outer motions length scale [26]. For zero pressure gradient (ZPG) turbulent BLs, validation of inner-outer region models with experimental results further support the theory of inner-outer region interaction [27]. These models rely on the basis of a coexistence between the universal inner region and the footprints of the outer motions. The effects of the outer motions are felt through both direct superposition and modulating the intensity of the near-wall self-sustaining dynamics [28]. The influence of the outer motions on the inner region can even extend to the viscous sublayer [29]. In addition to creating intermittency in the near-wall statistics, LSMs also locally modulate the turbulent/nonturbulent interface within BLs [30].

Decades of research have compiled a significant understanding of the structure of wall-bounded turbulence, but how to best leverage this knowledge base for effective modeling and flow control (e.g., drag reduction) remains an open question. Choi *et al.* [31] proposed an active flow control technique solely based on disturbing the near-wall coherent structures, decreasing the fluctuating and mean wall shear stress resulting in drag reduction of about 15%. However, the aforementioned control scheme loses its efficiency at higher Reynolds numbers [32]. A numerical simulation and skin friction decomposition by Deck *et al.* [33] and De Giovanetti *et al.* [34] revealed that at high Reynolds numbers, the explicit impact of LSMs in the outer layer increases the wall shear stress. Therefore, to obtain a robust, scalable drag reduction scheme, it is essential to manipulate the flow field in both inner and outer layers. This is one example demonstrating that the development of effective flow control schemes stands to benefit from analysis methods that can quantify the contribution of different turbulent scales on surface friction and heat flux, the typical engineering quantities of interest.

For fully developed internal flows such as channel or pipe flows, a second moment integral (or, equivalently, a triple integration) of the mean momentum equation provides a simple method for quantifying the effect of Reynolds stresses on the friction factor compared to an equivalent laminar flow [35,36]. The Fukagata-Iwamoto-Kasagi (FIK) equation has, for example, provided an important guidance for flow control in the context of internal flows [37]. A generalized form of the FIK equation for three-dimensional complex wall shapes was introduced by Peet and Sagaut [38]. For incompressible turbulent BLs, several derivations of the FIK equation were developed based on the triple integration [39,40]. Interestingly, the weighting of the Reynolds shear stress term in the resulting integral equation shows that turbulent fluctuations near the wall are more influential in the friction factor enhancement than those closer to the centerline. Instead of triple integration, a twofold repeated integration was proposed to remove the wall-normal distance weighting for incompressible and compressible turbulent BLs to decompose the skin friction and surface heat flux [41–43]. However, in the FIK equation and these variants based on double integration, the viscous term does not represent the laminar skin friction, i.e., the Blasius solution [44] for incompressible BLs. Thus, the FIK relation loses its clean interpretation when applied to BLs.

Several other relationships for BLs were introduced to decompose skin friction. Renard and Deck [45] proposed a relationship based on the turbulent kinetic energy budget equation, known as the RD equation. The RD equations emphasize the dominant role of the logarithmic layer on generation of turbulent skin friction. The RD equation was extended for compressible ZPG BLs [46] and applied to the direct numerical simulation (DNS) data to decompose the skin friction of supersonic [47,48], as well as hypersonic BLs with finite-rate chemistry effects [49]. Similar to the FIK equation,

the RD equation does not isolate the contribution of viscous effect (laminar flow). Thus, the interpretation of the RD equation is not based on the wall shear enhancement compared with a base laminar flow.

Recently, Elnahas and Johnson [50] developed the angular momentum integral (AMI) equation by integrating the first moment of momentum deficit equation for incompressible BLs. The AMI equation accomplishes for BLs what the FIK equation does for internal flows (pipes, channels). Specifically, it relates the skin-friction coefficient of any (e.g., turbulent) BL to the sum of an equivalent laminar skin-friction coefficient (as a function of a user-defined Reynolds number) plus an (unweighted) integral of the Reynolds shear stress, along with other terms (e.g., free-stream pressure gradients). In addition to the clear mathematical interpretation as enhancement or attenuation relative to an equivalent laminar BL, the AMI equation also has an intuitive physical explanation in terms of torques that reshape the mean velocity profile, changing its angular momentum (moment of momentum) and affecting the slope at the wall. Analogously, a first moment integral method for energy (temperature) equation was developed to obtain the moment of temperature integral (MTI) equation for incompressible BLs with heat transfer [51]. MTI provides a quantifying mapping between different flow phenomena, including turbulent contribution, and how they alter the Stanton number. The existing development of AMI and MTI equations has previously focused solely on incompressible BLs, so the application of this approach for compressible BLs is not yet clear.

The purpose of this paper is to derive and demonstrate how the AMI equation can be applied to compressible BLs of a calorically perfect gas. In addition, a moment of total enthalpy integral (MTEI) equation is introduced as an extension to the MTI equation previously developed for incompressible BLs [51]. The MTEI equation provides an interpretable relationship for the Stanton number in compressible BLs in terms of key flow physics, analogous to what AMI accomplishes for the skin friction coefficient. This integral-based approach provides another perspective for examining the effect of Mach number and wall cooling on turbulence in high-speed BLs with a particular focus on engineering-relevant surface quantities related to drag and heat transfer.

The paper is organized as follows. Section II derives the AMI equation for compressible BL flow of a calorically perfect gas and provides an intuitive interpretation for each term related to the skin-friction coefficient. In Sec. III, the MTEI equation for the Stanton number is obtained in a similar manner and a comprehensive interpretation of each flow feature is discussed. Then, Sec. IV briefly summarizes the DNS data set and the numerical methods to solve turbulent and self-similar laminar compressible BLs and demonstrate the use of the AMI and MTEI equations. Finally, in Section V, the AMI and MTEI equations are applied to analyze the DNS data for a range of edge Mach numbers and wall-temperature boundary conditions. Conclusions are given in Sec. VI.

## II. ANGULAR MOMENTUM INTEGRAL EQUATION FOR COMPRESSIBLE BOUNDARY LAYERS

The AMI equation has been previously derived and demonstrated for incompressible BLs by Ref. [50]. In this section, a more general form of the AMI equation is introduced, taking into account density and viscosity variation. The result provides a direct relationship that quantitatively maps flow physics throughout the BL based on their enhancement or attenuation of the skin friction coefficient relative to a baseline laminar BL.

### A. Derivation of the AMI equation

The derivation of the AMI equation for compressible flows is outlined in this subsection. The Reynolds-averaged conservation of mass and streamwise momentum for a statistically steady 2D

flow, respectively, yield

$$\frac{\partial(\bar{\rho}\tilde{u})}{\partial x} + \frac{\partial(\bar{\rho}\tilde{v})}{\partial y} = 0 \quad \text{and} \quad (1)$$

$$\frac{\partial(\bar{\rho}\tilde{u}\tilde{u})}{\partial x} + \frac{\partial(\bar{\rho}\tilde{u}\tilde{v})}{\partial y} = -\frac{\partial\bar{p}}{\partial x} + \frac{\partial}{\partial y}\left(\mu\frac{\partial\tilde{u}}{\partial y} - \bar{\rho}\tilde{u}''\tilde{v}''\right) + I_x, \quad (2)$$

where  $(\bar{\cdot})$  stands for the Reynolds averaging. Also,  $(\bar{\cdot})$  and  $(\cdot)''$  represent a density-weighted (Favre) averaged quantity and fluctuations with respect to the Favre averaging, respectively. In Eq. (2),  $u$ ,  $v$ , and  $p$  are the streamwise ( $x$ ) velocity, wall-normal ( $y$ ) velocity, and pressure, respectively. Also,  $\rho$  and  $\mu$  are the density and dynamic viscosity, respectively. Note,  $I_x$  represents the streamwise derivative terms neglected by the BL approximations. At the edge of the BL, assuming there is no wall-normal gradient and viscous effect, the streamwise momentum equation yields

$$\rho_e U_e \frac{dU_e}{dx} = -\frac{dP_e}{dx}, \quad (3)$$

where the subscript  $(\cdot)_e$  stands for the edge quantities like the edge velocity,  $U_e$ , and pressure,  $P_e$ . Subtracting Eq. (2) from Eq. (3) and adding  $U_e$  multiplied by Eq. (1) gives a transport equation for the mean streamwise velocity defect,

$$\frac{\partial(\bar{\rho}\tilde{u}(U_e - \tilde{u}))}{\partial x} + \frac{\partial(\bar{\rho}\tilde{v}(U_e - \tilde{u}))}{\partial y} = -(\rho_e U_e - \bar{\rho}\tilde{u})\frac{dU_e}{dx} + \frac{\partial}{\partial y}\left(\bar{\rho}\tilde{u}''\tilde{v}'' - \mu\frac{\partial\tilde{u}}{\partial y}\right) - I_2, \quad (4)$$

where the terms neglected by the statistically stationary BL approximations (including the streamwise gradient of the edge and mean pressure difference) are gathered in  $I_2$ . Integration of Eq. (4) across the BL,  $\int_0^\infty [\cdot] dy$  yields the von Kármán momentum integral equation,

$$\frac{C_f}{2} = \frac{d\delta_2}{dx} + \left(2 + \frac{\delta_1}{\delta_2} + \frac{U_e}{\rho_e} \frac{d\rho_e}{dU_e}\right) \frac{\delta_2}{U_e} \frac{dU_e}{dx} + \mathcal{I}_2, \quad (5)$$

where the skin-friction coefficient,  $C_f = 2\bar{\tau}_w/\rho_e U_e^2$ , is the nondimensional mean wall shear stress,  $\tau_w = \mu_w(\partial u/\partial y)_w$ . For isentropic edge flow,  $(U_e/\rho_e)\partial\rho_e/\partial U_e = -M_e^2$ . Moreover,  $\mathcal{I}_2$  is the outcome of the integration of  $I_2$  and can be safely neglected for most thin BL flows. The momentum and displacement thicknesses for compressible BLs are, respectively,

$$\delta_2 \equiv \int_0^\infty \frac{\bar{\rho}}{\rho_e} \frac{\tilde{u}}{U_e} \left(1 - \frac{\tilde{u}}{U_e}\right) dy \quad \text{and} \quad \delta_1 \equiv \int_0^\infty \left(1 - \frac{\bar{\rho}}{\rho_e} \frac{\tilde{u}}{U_e}\right) dy. \quad (6)$$

Equation (5) is valid for both laminar and turbulent regimes; however, the contribution of turbulence is implicit. In other words, Eq. (5) does not provide any explicit representation of how turbulence impacts the skin friction coefficient.

The AMI equation is derived by multiplying Eq. (4) by  $(y - \ell(x))$ —the first moment—and integrating across the BL,  $\int_0^\infty \{y - \ell(x)\} [\cdot] dy$ . Applying the no-slip and no-penetration boundary conditions at the wall, the AMI relation reads

$$\begin{aligned} \frac{C_f}{2} = & \frac{1}{\text{Re}_\ell} + \frac{1}{\ell} \int_0^\infty \frac{-\bar{\rho}\tilde{u}''\tilde{v}''}{\rho_e U_e^2} dy + \left\{ \frac{d\delta_2^\ell}{dx} - \frac{\delta_2 - \delta_2^\ell}{\ell} \frac{d\ell}{dx} \right\} + \frac{\delta_2^v}{\ell} + \frac{1}{\ell} \int_0^\infty \frac{(\mu - \mu_{\text{ref}})\frac{\partial\tilde{u}}{\partial y}}{\rho_e U_e^2} dy \\ & + \left(2 + \frac{\delta_1^\ell}{\delta_2^\ell} + \frac{U_e}{\rho_e} \frac{d\rho_e}{dU_e}\right) \frac{\delta_2^\ell}{U_e} \frac{dU_e}{dx} + \mathcal{I}_2^\ell, \end{aligned} \quad (7)$$

where  $\mu_{\text{ref}}$  is a reference viscosity to define the Reynolds number of a compressible BL,  $\text{Re}_\ell = U_e \rho_e \ell / \mu_{\text{ref}}$ , and  $\mathcal{I}_2^\ell$  is generated by integration of the first moment of  $I_2$ . An appropriate definition of the length scale  $\ell$  to isolate the laminar friction is given in Eqs. (13), followed by other alternative options in Sec. II B 1. Also, the full derivation of the AMI equation, Eq. (7), is provided in Appendix A. The AMI equation for compressible BLs, Eq. (7), was independently introduced by

TABLE I. Physical description and terminology of the flow phenomena in the AMI equation.

AMI term	Mathematical expression	→	Description
(I)	$\frac{1}{\text{Re}_\ell}$	→	skin friction coefficient of an equivalent laminar BL at matched $\text{Re}_\ell$
(II)	$\frac{1}{\ell} \int_0^\infty \frac{-\bar{\rho} \tilde{u}'' v''}{\rho_e U_e^2} dy$	→	turbulent torque by Reynolds shear stress
(III)	$\frac{d\delta_2^\ell}{dx} - \frac{\delta_2 - \delta_2^\ell}{\ell} \frac{d\ell}{dx}$	→	streamwise growth of angular momentum thickness
(IV)	$\frac{\delta_2^v}{\ell}$	→	torque by mean wall-normal transport
(V)	$\frac{1}{\ell} \int_0^\infty \frac{(\mu - \mu_{\text{ref}}) \frac{\partial \tilde{u}}{\partial y}}{\rho_e U_e^2} dy$	→	deviation from reference viscosity
(VI)	$\frac{1}{U_e} \frac{dU_e}{dx} (\delta_1^\ell + 2\delta_2^\ell) + \frac{1}{\rho_e} \frac{d\rho_e}{dx} \delta_2^\ell$	→	edge pressure gradient torque
(VII)	$\mathcal{I}_2^\ell$	→	negligible terms, departure from BL assumptions

Kianfar *et al.* [52] and Xu *et al.* [53]. Note that Ref. [53] used a slightly different treatment of the mean viscosity variation, basing their treatment on the Reynolds number using the edge viscosity.

The angular momentum and displacement thicknesses introduced in Eq. (7) are, respectively,

$$\delta_2^\ell \equiv \int_0^\infty \left(1 - \frac{y}{\ell}\right) \frac{\bar{\rho}}{\rho_e} \frac{\tilde{u}}{U_e} \left(1 - \frac{\tilde{u}}{U_e}\right) dy \quad \text{and} \quad \delta_1^\ell \equiv \int_0^\infty \left(1 - \frac{y}{\ell}\right) \left(1 - \frac{\bar{\rho}}{\rho_e} \frac{\tilde{u}}{U_e}\right) dy. \quad (8)$$

Finally, Eq. (7) also introduces the wall-normal momentum thickness:

$$\delta_2^v \equiv \int_0^\infty \frac{\bar{\rho}}{\rho_e} \frac{\tilde{v}}{U_e} \left(1 - \frac{\tilde{u}}{U_e}\right) dy. \quad (9)$$

Following the BL theory, the streamwise direction,  $x$ , may be interpreted as a timelike variable. In this perspective, Eq. (7) may be seen as an integral conservation principle for angular momentum about  $y = \ell(x)$ . As such, the AMI equation represents the sum of torques equal to the growth of the BL's AMI,  $d\delta_2^\ell/dx$ .

### B. Interpretation of the AMI equation

The terms appearing on the right-hand side of the AMI equation, Eq. (7), represent various physical flow phenomena influencing the skin-friction coefficient. A succinct physical description of each term is given in Table I. A more detailed discussion of the terms is given in each of the following paragraphs below. Since the AMI equation arises from the first moment of the velocity defect transport equation, the flow phenomena on the right-hand side of Eq. (7) may be interpreted as torques. Figure 1 presents a schematic of how these flow phenomena may be seen as torques that redistribute momentum relative to  $y = \ell(x)$ , reshaping the mean velocity profile. For example, the Reynolds shear stress acts as a counterclockwise torque with respect to  $y = \ell(x)$  which redistributes momentum toward the wall (more precisely, velocity defect away from the wall), causing an enhancement in the skin friction. As a different example, an adverse pressure gradient acts as a clockwise torque, redistributing momentum away from the wall (velocity defect toward the wall) and decreasing the skin friction.

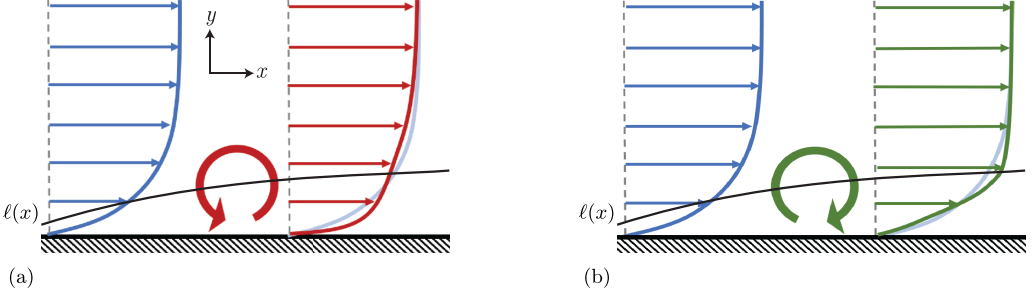


FIG. 1. Schematic of applying torque with respect to axis  $\ell(x)$  (black solid line) to the blue velocity profile: (a) applying a counterclockwise torque and (b) applying a clockwise torque.

### 1. Viscous force and laminar friction coefficient, (I) and (VI)

In the AMI equation, the skin-friction coefficient,  $C_f$ , the *laminar* friction, and viscous *deviation* terms originate from the first-order moment of viscous force (viscous torque) about  $y = \ell(x)$ :

$$T_{v,\ell} = \int_0^\infty (y - \ell) \left[ \frac{\partial}{\partial y} \left( \overline{\mu \frac{\partial u}{\partial y}} \right) \right] dy = \ell \tau_w - \mu_{\text{ref}} U_e - \int_0^\infty \overline{(\mu - \mu_{\text{ref}}) \frac{\partial u}{\partial y}} dy. \quad (10)$$

If we choose the reference viscosity to be the shear stress weighted viscosity,  $\mu_{\text{ref}} = \mu_2$ , defined as

$$\mu_2 = \frac{\int_0^\infty \overline{\mu \frac{\partial u}{\partial y}} dy}{\int_0^\infty \overline{\frac{\partial u}{\partial y}} dy} = \frac{1}{U_e} \int_0^\infty \overline{\mu \frac{\partial u}{\partial y}} dy, \quad (11)$$

the *deviation* term (V) will vanish. In that particular case, the viscous torque becomes

$$T_{v,\ell} = \rho_e U_e^2 \ell \left( \frac{C_f}{2} - \frac{1}{\text{Re}_\ell} \right). \quad (12)$$

From Eq. (12), if  $\ell$  is chosen such that  $C_f/2 = 1/\text{Re}_\ell = \mu_2/(\rho_e U_e \ell)$  for a ZPG laminar BL solution, then the viscous torque about that  $\ell$  vanishes,  $T_{v,\ell} = 0$ . The length scale  $\ell$  mathematically connects two BLs, the BL to be analyzed, and the baseline ZPG laminar BL it is compared against. The interpretation of the laminar term becomes particularly profitable when the length scale  $\ell$  is tied to a thickness measurement of the BL, e.g.,  $\delta_2$ ,  $\delta_1$ , or  $\sqrt{vx}/U_e$ . Given the physical significance of the momentum thickness stemming from the momentum integral equation, Eq. (5),  $\ell \sim \delta_2$  is a natural choice that has provided insight for incompressible BLs [50]. With this choice,

$$\frac{C_f}{2} = \frac{1}{\text{Re}_\ell} = \frac{c_2 \mu_{\text{ref}}}{U_e \rho_e \delta_2} \quad \text{and} \quad \ell = \delta_2 / c_2, \quad (13)$$

where  $c_2$  is a constant determined by solving self-similar laminar compressible (or incompressible) BL equations. From Eqs. (13), one can extract the appropriate length scale  $\ell$ , representing the center of action of the viscous force for an equivalent laminar BL with the same  $\text{Re}_{\delta_2} = \rho_e U_e \delta_2 / \mu_{\text{ref}}$ . Alternative choices are possible, such as tying the length scale to  $\ell \sim \delta_1$  or  $\ell \sim \sqrt{vx}/U_e$ , which would correspond to the center of action for the viscous force in a laminar BL at the same  $\text{Re}_{\delta_1}$  or  $\text{Re}_x$ , respectively [50,53]. Therefore,  $\ell = \delta_2 / c_2$  isolates in a single term of the AMI equation the equivalent skin friction coefficient of a laminar BL having the same  $\text{Re}_{\delta_2} = \rho_e U_e \delta_2 / \mu_{\text{ref}}$ . In other words,  $2/\text{Re}_\ell$  represents the skin-friction coefficient if the flow was a ZPG laminar BL at the same momentum thickness Reynolds number. As a result, all other terms in the AMI equation can be interpreted as augmentations or attenuations of the skin friction coefficient compared to the laminar case.

Note that the laminar solution of the skin friction coefficient to determine  $c_2$  may come from an incompressible (e.g., Blasius) or fully compressible formulation. If a solution to the Blasius equation is used ( $c_2 \approx 0.22$ ), then the AMI equation represents the comparison of a general turbulent compressible BL with an incompressible laminar one. If a more general compressible formulation of the self-similar BL equations is used [12], then the AMI equation can be interpreted as a comparison with a baseline ZPG laminar BL at the same edge Mach number,  $M_e$ , and wall-edge temperature ratio  $T_w/T_e$ — provided the self-similar solution for  $c_2$  matches those quantities, i.e.,  $c_2 = c_2(M_e, T_w/T_e)$ .

In addition to choosing the reference length scale (e.g.,  $\ell \sim \delta_2$  or  $\ell \sim \delta_1$ ) and the reference BL formulation (incompressible or compressible), the use of the AMI equation also allows for choosing different reference viscosities. As noted above, there is one particularly advantageous choice for the AMI equation,  $\mu_{\text{ref}} = \mu_2$ , because it causes the *deviation* term to vanish. With the choice of  $\mu_2$ , the Reynolds number used for similarity with the baseline laminar BL is

$$\text{Re}_2 = \frac{U_e \rho_e \delta_2}{\mu_2} = \frac{\int_0^\infty \bar{\rho} \tilde{u} (U_e - \tilde{u}) dy}{\int_0^\infty \mu \frac{\partial \tilde{u}}{\partial y} dy} = \frac{\int_0^x \bar{\tau}_w(\xi) d\xi}{\int_0^\infty \mu \frac{\partial \tilde{u}}{\partial y} dy}, \quad (14)$$

where  $x = 0$  is the start of the BL. The numerator of  $\text{Re}_2$  is the net streamwise flux of velocity defect in the boundary layer. Using the momentum integral equation, Eq. (5), this is equal to the upstream-integrated mean wall shear stress (in the absence of an edge pressure gradient). The denominator is the wall-normal integral of the viscous stress across the BL.

One alternative to  $\mu_2$  would be the wall viscosity,  $\mu_w$ . These two probably do not differ much for adiabatic walls but can differ significantly for strong wall cooling. In principle, the edge viscosity,  $\mu_e$ , could also be chosen. In the end, the choices of length scale and reference viscosity combine to determine the particular interpretation of the AMI equation as a comparison of skin friction coefficient with an equivalent laminar BL with matched  $\text{Re}_\ell = \rho_e U_e \ell / \mu_{\text{ref}}$ .

## 2. Reynolds shear stress and turbulent torque (II)

The second term on the right-hand side of the AMI equation is the torque due to the Reynolds shear stress,  $-\bar{\rho} u'' v''$ . The Reynolds stress does not appear explicitly in the momentum integral equation, Eq. (5), because it evaluates to zero at both boundaries (wall and edge). In contrast, by integrating the first moment of the velocity defect transport equation, the integral of the Reynolds shear stress appears as an effective torque redistributing velocity defect in the wall-normal direction:

$$\int_0^\infty (y - \ell) \frac{\partial(\bar{\rho} \tilde{u}'' v'')}{\partial y} dy = - \int_0^\infty \bar{\rho} \tilde{u}'' v'' dy. \quad (15)$$

This *turbulent torque* explicitly quantifies how turbulence enhances the BL's friction relative to the baseline laminar BL by bringing higher momentum fluid toward the wall. It is worth mentioning that, in the AMI equation, in contrast to the FIK relation for internal flows [35], the contribution of Reynolds shear stress to the skin-friction coefficient is unweighted. The physical interpretation of the weighting (or lack thereof) in the Reynolds shear stress integral is discussed in detail in Ref. [50].

For compressible flows, the velocity covariance is weighted by the mean density, signifying the role of density in the turbulent transport of momentum. The impact of density variation on the wall-normal turbulent flux is not specific to the definition of Favre averaging. In general, the momentum (and hence momentum flux) is proportional to the local density, regardless of the averaging method. In fact, the difference between  $\overline{u'v'}$  and  $\tilde{u}''v''$  was not found to be significant in the present paper. The role of density variation in altering the turbulence stresses may be encapsulated by a stress-weighted

density,

$$\rho_2 = \frac{\int_0^\infty \bar{\rho} \widetilde{u''v''} dy}{\int_0^\infty \widetilde{u''v''} dy}, \quad (16)$$

such that, by definition, the turbulent torque may be written as  $-\rho_2 \int_0^\infty \widetilde{u''v''} dy$ . For most BL flows,  $-\widetilde{u''v''} > 0$ , so the turbulent torque defined here is typically positive (enhancement of wall shear stress).

### 3. Streamwise growth of momentum thickness (III)

Integrating the first moment of the streamwise momentum deficit yields

$$-\int_0^\infty (y - \ell) \frac{\partial}{\partial x} \left( \frac{\bar{\rho}}{\rho_e} \frac{\tilde{u}}{U_e} \left( 1 - \frac{\tilde{u}}{U_e} \right) \right) dy = \ell \frac{d\delta_2^\ell}{dx} - (\delta_2 - \delta_2^\ell) \frac{d\ell}{dx}. \quad (17)$$

The momentum thickness  $\delta_2$  from the classical momentum integral equation, Eq. (5), represents the net streamwise flux of streamwise velocity defect. Likewise,  $\delta_2^\ell$ , the angular momentum thickness, represents the first moment about  $y = \ell(x)$  of the streamwise velocity defect flux. Equation (17) represents the rate at which the angular momentum thickness grows relative to the growth rate of  $\ell$ . The choice of length scale,  $\ell$ , plays an important quantitative role in this term. The angular momentum thickness,  $\delta_2^\ell$ , is a signed quantity and can be negative or positive depending on the choice of  $\ell$ . One way to interpret Eq. (17) is to think of it as representing the rate of change of the angular momentum, with the streamwise coordinate as a timelike variable. As such, it is the resultant term from all of the torques acting on the BL profile, including all other terms in Table I as well as the wall shear stress itself from the left-hand side of the AMI equation, Eq. (7). Thus, the angular momentum thickness can be thought of as absorbing any imbalance of torques at a given streamwise location.

### 4. Mean wall-normal torque (IV)

The *mean wall-normal* torque in the AMI equation originates from the flux of velocity defect carried by the mean wall-normal flow:

$$-\int_0^\infty (y - \ell) \frac{\partial}{\partial y} \left( \frac{\bar{\rho}}{\rho_e} \frac{\tilde{v}}{U_e} \left( 1 - \frac{\tilde{u}}{U_e} \right) \right) dy = \delta_2^v. \quad (18)$$

This term represents the wall-normal flux of streamwise velocity defect, typically positive in most BL conditions. When  $\tilde{v}$  is positive, as is typical in BLs, this acts to increase the skin friction because the effect is to transport velocity defect away from the wall, increasing the near-wall velocity, so it looks like a counterclockwise torque in the AMI equation. In special cases, when  $\tilde{v} \leq 0$ , the mean wall-normal velocity transports velocity defect toward the wall to attenuate the skin friction. For example, a reversal of mean wall-normal flux has been observed for transitional BLs in the incompressible regime [50].

### 5. Nonzero edge pressure gradient (VI)

The torque due to edge pressure gradient originates from a nonzero streamwise derivation of edge velocity,  $U_e$ , and/or density,  $\rho_e$ . A favorable edge pressure gradient accelerates the edge velocity, damping the velocity defect in the BL and acting as a counterclockwise torque which tends to increase the skin friction, Fig. 1(a). In contrast, an adverse pressure gradient reduces the wall shear stress by acting as a clockwise torque with respect to  $y = \ell(x)$ , Fig. 1(b). In this paper, only ZPG BLs will be considered, so this term is negligible for all cases shown here. Future work will examine the effect of edge pressure gradients using the AMI equation.

### 6. Departure from BL approximations (VII)

Torque caused by the terms corresponding to derivatives with respect to streamwise direction and variation of mean pressure across the BL are included in  $\mathcal{I}_2^t$ . For most BLs, the contribution of these terms are expected to be negligible. The *negligible terms*, however, might need to be accounted for in some important scenarios, such as transitional flows and flows in the vicinity of the BL separation or shock-BL interactions.

## III. A MOMENT OF TOTAL ENTHALPY INTEGRAL EQUATION

In a previous study, the concept of the AMI equation was extended to study heat transfer in incompressible BLs [51], analogous to the AMI equation for the skin-friction coefficient. The resulting MTI equation relates the surface heat flux to various flow physics through the BL. In this section, this approach is generalized to form the MTEI equation for compressible BLs, taking into account variations in density, viscosity, and thermal conductivity.

### A. Derivation of the MTEI equation

By taking a similar approach as in Sec. II, we obtain the MTEI equation from the total enthalpy equation. The Reynolds-averaged total enthalpy equation for a statistically stationary 2D BL reads

$$\frac{\partial}{\partial x}(\overline{\rho} \tilde{u} \tilde{H}) + \frac{\partial}{\partial y}(\overline{\rho} \tilde{v} \tilde{H}) = \frac{\partial}{\partial y} \left( \overline{\kappa} \frac{\partial T}{\partial y} + \overline{\mu u} \frac{\partial u}{\partial y} - \overline{\rho v'' \tilde{H}''} \right) + I_H, \quad (19)$$

in which the Favre averaging is implemented. In Eq. (19),  $H = c_p T_o = c_p T + u^2/2$  is total enthalpy (by neglecting contributions of wall-normal and spanwise velocities by invoking standard BL arguments) and  $T$  is temperature. While the (dynamic) viscosity ( $\mu$ ) and thermal conductivity ( $\kappa$ ) are assumed to vary with temperature, Prandtl number,  $\text{Pr} = \mu c_p / \kappa$ , and specific heat capacity,  $c_p$ , are approximated as constants in this paper, though this assumption can be straightforwardly relaxed to address more general scenarios. In Eq. (19), the terms that are neglected in BL approximation are collected in  $I_H$ . Subtracting Eq. (19) from  $H_e$  times the continuity equation, Eq. (1), a transport equation for the total enthalpy defect is achieved:

$$\frac{\partial}{\partial x}(\overline{\rho} \tilde{u} (H_e - \tilde{H})) + \frac{\partial}{\partial y}(\overline{\rho} \tilde{v} (H_e - \tilde{H})) = - \frac{\partial}{\partial y} \left( \overline{\kappa} \frac{\partial T}{\partial y} + \overline{\mu u} \frac{\partial u}{\partial y} - \overline{\rho v'' \tilde{H}''} \right) - I_H. \quad (20)$$

The total enthalpy at the BL edge,  $H_e$ , is assumed constant in the streamwise direction (i.e., assuming adiabatic flow outside the BL). Integrating Eq. (20) across the BL yields the (classic) integral equation for the Stanton number

$$\text{St} = \frac{d\delta_H}{dx} + \left( 1 + \frac{U_e}{\rho_e} \frac{\partial \rho_e}{\partial U_e} \right) \frac{\delta_H}{U_e} \frac{dU_e}{dx} + \frac{\delta_H}{H_{\text{ref}} - H_w} \frac{d(H_{\text{ref}} - H_w)}{dx} + \mathcal{I}_H, \quad (21)$$

where the Stanton number (St) and total enthalpy thickness ( $\delta_H$ ) are defined as follows:

$$\text{St} \equiv \frac{\overline{q_w}}{\rho_e U_e (H_{\text{ref}} - H_w)}, \quad \delta_H \equiv \int_0^\infty \frac{\overline{\rho}}{\rho_e} \frac{\tilde{u}}{U_e} \left( \frac{H_e - \tilde{H}}{H_{\text{ref}} - H_w} \right) dy. \quad (22)$$

In the above,  $q_w = -\kappa_w (\partial T / \partial y)_w$  is the wall heat flux. Typically negligible for BLs,  $\mathcal{I}_H$  is the result of integration of  $I_H$ . Equation (21) is valid for laminar, transitional, and turbulent flows, yet one cannot determine the explicit contribution of fluctuations (or perturbations) on surface heat flux. In contrast, taking a similar approach as the AMI equation, we multiply Eq. (20) by a length scale,  $(y - \ell)$  (as the first moment), then integrate the whole equation across the BL. Implementing the wall and edge boundary conditions, we obtain the MTEI equation for high-speed

compressible BLs:

$$\begin{aligned}
 \text{St} = & \frac{1}{\text{Pr}_{\text{ref}}\text{Re}_\ell} + \frac{1}{\ell} \int_0^\infty \frac{-\bar{\rho}\widetilde{v''H''}}{\rho_e U_e (H_{\text{ref}} - H_w)} dy + \left\{ \frac{d\delta_H^\ell}{dx} - \frac{\delta_H - \delta_H^\ell}{\ell} \frac{d\ell}{dx} \right\} + \frac{\delta_H^v}{\ell} \\
 & + \frac{1}{\ell} \int_0^\infty \frac{(\kappa - \kappa_{\text{ref}})\frac{\partial T}{\partial y} + (\mu - \mu_{\text{ref}})u\frac{\partial u}{\partial y}}{\rho_e U_e (H_{\text{ref}} - H_w)} dy + \left( 1 + \frac{U_e}{\rho_e} \frac{\partial \rho_e}{\partial U_e} \right) \frac{\delta_H^\ell}{U_e} \frac{dU_e}{dx} \\
 & + \frac{\delta_H^\ell}{H_{\text{ref}} - H_w} \frac{d(H_{\text{ref}} - H_w)}{dx} + \mathcal{I}_H^\ell, \tag{23}
 \end{aligned}$$

where the left-hand side is the Stanton number defined in Eqs. (22). The basis of choosing an appropriate length scale  $\ell$  for the MTEI equation is discussed in Sec. III B 1. In particular, to isolate the laminar Stanton number (like in this paper),  $\ell$  is defined in Eq. (30). The MTEI equation, Eq. (23), introduces the moment of total enthalpy thickness and mean wall-normal enthalpy thickness as

$$\delta_H^\ell \equiv \int_0^\infty \left( 1 - \frac{y}{\ell} \right) \frac{\bar{\rho}}{\rho_e} \frac{\tilde{u}}{U_e} \left( \frac{H_e - \tilde{H}}{H_{\text{ref}} - H_w} \right) dy, \quad \delta_H^v \equiv \int_0^\infty \frac{\bar{\rho}}{\rho_e} \frac{\tilde{v}}{U_e} \left( \frac{H_e - \tilde{H}}{H_{\text{ref}} - H_w} \right) dy, \tag{24}$$

respectively. The total enthalpy thickness,  $\delta_H$ , is recovered in the limit of  $\ell \rightarrow \infty$ . Finally,  $\mathcal{I}_H^\ell$  in Eq. (23), arises from the integration of the first moment of  $I_H$ .

In Eq. (23),  $\kappa_{\text{ref}}$  and  $\mu_{\text{ref}}$  are the reference conductivity and viscosity, respectively. The reference conductivity and viscosity are related via a reference Prandtl number,  $\text{Pr}_{\text{ref}} = c_p \mu_{\text{ref}} / \kappa_{\text{ref}}$ . It is not necessary to choose  $\text{Pr}_{\text{ref}} = \text{Pr}$ , even for constant Pr flow. Instead, the reference Prandtl number should be chosen based on the desired reference enthalpy:

$$H_{\text{ref}} = c_p(T_e - T_w) + \text{Pr}_{\text{ref}} \frac{U_e^2}{2}. \tag{25}$$

Thus, the reference Prandtl number acts as a sort of reference recovery factor for defining the Stanton number.

A common definition of the Stanton number is based on the difference between the adiabatic wall temperature,  $T_{\text{aw}}$ , and wall temperature,  $T_w$ , that is,  $\text{St} = \bar{q}_w / \rho_e U_e (H_{\text{aw}} - H_w)$ . Such a definition can be facilitated with the choice of  $\text{Pr}_{\text{ref}} = r_{\text{ref}}$ , the reference recovery factor for defining an adiabatic wall temperature. However, it is well-known that the recovery factor for laminar and turbulent BLs can be quite different, e.g.,  $\text{Pr}^{1/2}$  for laminar BLs and approximately  $\text{Pr}^{1/3}$  for turbulent BLs [12]. This complicates the interpretation of the MTEI equation, in particular, the first term, which should represent the Stanton number of an equivalent laminar BL that serves as a reference for the transitional or turbulent BL under consideration. Thus, it is not clear how to choose the reference recovery factor. (Often for BLs in the hypersonic regime with chemical and/or thermal nonequilibrium, the heat flux coefficient is defined based on the edge kinetic energy,  $C_q = \bar{q}_w / \rho_e U_e^3$  [54].)

Instead, the authors believe that the interpretation of the MTEI equation is more clear if the edge stagnation enthalpy is used in the denominator of the Stanton number, corresponding to the choice of  $\text{Pr}_{\text{ref}} = 1$ . With this choice, the denominator includes the maximum total enthalpy difference,  $H_e - H_w$ , available to supply energy to the wall (in the form of surface heat flux). This definition does allow for negative Stanton numbers in the case of nonunity recovery factors, but such negative Stanton numbers are interpretable as net energy flux opposite the global driving energy difference. The effect of turbulence to increase the recovery factor (adiabatic wall temperature) can thus be included within the broader analysis without causing interpretive difficulties. Thus, the Stanton number definition used in this paper is given by Eqs. (22), equivalent to the choice of  $\text{Pr}_{\text{ref}} = 1$ . Other choices are possible and may be the subject of future research.

TABLE II. Physical description and terminology of the flow phenomena in the MTEI equation.

MTEI term	Mathematical expression	→	Description
(I)	$\frac{1}{\text{Pr}_{\text{ref}}\text{Re}_\ell}$	→	the Stanton number of an equivalent <i>laminar</i> BL at matched $\text{Re}_\ell$
(II)	$\frac{1}{\ell} \int_0^\infty \frac{-\bar{\rho}v''\bar{H}'}{\rho_e U_e (H_{\text{ref}} - H_w)} dy$	→	<i>turbulent flux</i> integral, turbulent transport of total enthalpy
(III)	$\frac{d\delta_H^\ell}{dx} - \frac{\delta_H - \delta_H^\ell}{\ell} \frac{d\ell}{dx}$	→	<i>streamwise growth</i> of the first moment of total enthalpy thickness
(IV)	$\frac{\delta_H^v}{\ell}$	→	flux by <i>mean wall-normal</i> transport
(V)	$\frac{1}{\ell} \int_0^\infty \frac{(\kappa - \kappa_{\text{ref}}) \frac{\partial T}{\partial y} + (\mu - \mu_{\text{ref}}) u \frac{\partial u}{\partial y}}{\rho_e U_e (H_{\text{ref}} - H_w)} dy$	→	<i>deviation</i> from reference viscous transport
(VI)	$(1 + \frac{U_e}{\rho_e} \frac{\partial \rho_e}{\partial U_e}) \frac{\delta_H^\ell}{U_e} \frac{dU_e}{dx}$	→	<i>edge pressure gradient flux</i>
(VII)	$\frac{\delta_H^\ell}{H_{\text{ref}} - H_w} \frac{d(H_{\text{ref}} - H_w)}{dx}$	→	flux by <i>wall-temperature variation</i>
(VIII)	$\mathcal{I}_H^\ell$	→	<i>negligible terms</i>

## B. Interpretation of the MTEI equation

The right-hand side of the MTEI equation, Eq. (23), consists of several terms representing a mapping of flow phenomena based on how they alter the Stanton number. A physical description of each flow feature in the MTEI equation is discussed in Table II. Moreover, a detailed discussion of these flow phenomena is given in the proceeding paragraphs. The MTEI equation is derived from the first moment of the total enthalpy deficit transport equation that involves both internal and kinetic energy transport mechanisms. Thus, we interpret the flow phenomena on the right-hand side of Eq. (23) as fluxes of total enthalpy, or redistribution of the total enthalpy profile.

### 1. Viscous flux and the laminar Stanton number, (I) and (V)

In the MTEI equation, the Stanton number, *laminar* flux, and *deviation* originate from

$$\begin{aligned} & \int_0^\infty (y - \ell) \left[ \frac{\partial}{\partial y} \left( \kappa \frac{\partial T}{\partial y} + \mu u \frac{\partial u}{\partial y} \right) \right] dy \\ & = \ell q_w - \frac{\kappa_{\text{ref}}}{c_p} (H_{\text{ref}} - H_w) - \int_0^\infty \left( (\kappa - \kappa_{\text{ref}}) \frac{\partial T}{\partial y} + (\mu - \mu_{\text{ref}}) u \frac{\partial u}{\partial y} \right) dy. \end{aligned} \quad (26)$$

One can merge all the viscous (laminar) effects in a single term,  $1/\text{Pr}_{\text{ref}}\text{Re}_\ell$ , by choosing the reference conductivity as  $\kappa_{\text{ref}} = \kappa_H$  (i.e., reference viscosity as  $\mu_{\text{ref}} = \mu_H$ ), where

$$\kappa_H = \frac{\int_0^\infty \overline{\kappa (c_p \frac{\partial T}{\partial y} + \text{Pr} u \frac{\partial u}{\partial y})} dy}{\int_0^\infty \overline{(c_p \frac{\partial T}{\partial y} + \text{Pr}_{\text{ref}} u \frac{\partial u}{\partial y})} dy} = \frac{\int_0^\infty \overline{(\kappa \frac{\partial T}{\partial y} + \mu u \frac{\partial u}{\partial y})} dy}{T_{\text{ref}} - T_w}, \quad (27)$$

$$\mu_H = \frac{\int_0^\infty \overline{\mu (\frac{c_p}{\text{Pr}} \frac{\partial T}{\partial y} + u \frac{\partial u}{\partial y})} dy}{\int_0^\infty \overline{(\frac{c_p}{\text{Pr}_{\text{ref}}} \frac{\partial T}{\partial y} + u \frac{\partial u}{\partial y})} dy} = \frac{\text{Pr}_{\text{ref}} \int_0^\infty \overline{(\kappa \frac{\partial T}{\partial y} + \mu u \frac{\partial u}{\partial y})} dy}{c_p (T_{\text{ref}} - T_w)} = \frac{\text{Pr}_{\text{ref}}}{c_p} \kappa_H, \quad (28)$$

where  $T_{\text{ref}} = H_{\text{ref}}/c_p$  is the adiabatic wall temperature,  $T_{\text{ref}} = T_{\text{aw}}$ , for  $\text{Pr}_{\text{ref}} = r_{\text{ref}}$  or the edge stagnation temperature,  $T_{\text{ref}} = T_{o,e}$ , for the choice  $\text{Pr}_{\text{ref}} = 1$ . With such reference values, the *deviation* term (V) will vanish.  $\mu_H$  can be interpreted as a viscosity balancing between molecular conduction

and viscous dissipation of kinetic energy. Hence,

$$\rho_e U_e (H_e - H_w) \ell \left( \text{St} - \frac{1}{\text{Pr}_{\text{ref}} \text{Re}_\ell} \right) = 0. \quad (29)$$

For ZPG compressible BLs,

$$\text{St} = \frac{1}{\text{Pr}_{\text{ref}} \text{Re}_\ell} = \frac{c_H \kappa_H}{\rho_e c_p U_e \delta_H}, \quad \text{and} \quad \ell = \delta_H / c_H, \quad (30)$$

where  $c_H$  is a constant calculated by solving self-similar ZPG laminar compressible (or incompressible) momentum and energy equations. Implementing the definition of  $\ell$  according to Eq. (30) the laminar  $\text{St}$  is precisely equal to  $1/\text{Pr}_{\text{ref}} \text{Re}_\ell$  at specific  $\delta_H(x)$ . Together, the choice of  $\delta_H$  and  $\kappa_H$  as the reference length and reference transport coefficient, respectively, the Peclet number used for similarity with the baseline laminar BL is

$$\text{Pe}_H = \frac{U_e \rho_e c_p \delta_H}{\kappa_H} = \frac{\int_0^\infty \bar{\rho} \tilde{u} (H_e - \tilde{H}) dy}{\int_0^\infty (\kappa \frac{\partial T}{\partial y} + \mu u \frac{\partial u}{\partial y}) dy} = \frac{\int_0^x \bar{q}_w(\xi) d\xi}{\int_0^\infty (\kappa \frac{\partial T}{\partial y} + \mu u \frac{\partial u}{\partial y}) dy}. \quad (31)$$

The numerator is the streamwise flux of total enthalpy defect. Using the total enthalpy integral equation, Eq. (21), this is equal to the upstream-integrated wall heat flux. The denominator is the net wall normal flux of total enthalpy due to viscous and conductive transport.

### 2. Turbulent total enthalpy flux (II)

The second term on the right-hand side of the MTEI equation is the flux due to covariance of wall-normal velocity and total enthalpy,  $-\bar{\rho} \widetilde{H'' v''}$ . By integrating the first moment of the wall-normal derivative of the turbulence covariance,

$$\int_0^\infty (y - \ell) \frac{\partial (\bar{\rho} \widetilde{H'' v''})}{\partial y} dy = - \int_0^\infty \bar{\rho} \widetilde{H'' v''} dy, \quad (32)$$

we obtain the explicit contribution of the turbulent flux of total enthalpy (*turbulent flux*) to the surface heat flux. Naturally, the internal and kinetic energies are embedded into total enthalpy. Therefore, the covariance of wall-normal velocity and total enthalpy can be further decomposed to quantify the role of enthalpy and kinetic energies on *turbulent flux*. Equation (32) is rewritten as

$$\int_0^\infty \bar{\rho} \widetilde{H'' v''} dy = \int_0^\infty \bar{\rho} \left( c_p \widetilde{T'' v''} + \widetilde{u u'' v''} + \frac{1}{2} \widetilde{u'' u'' v''} \right) dy, \quad (33)$$

where  $c_p \bar{\rho} \widetilde{T'' v''}$ ,  $\bar{\rho} \widetilde{u u'' v''}$ , and  $\bar{\rho} \widetilde{u'' u'' v''} / 2$  are wall-normal turbulent fluxes of enthalpy, mean kinetic energy, and turbulent kinetic energy, respectively. For high Mach number (supersonic and hypersonic) BLs, the turbulent transport of the mean kinetic energy,  $\bar{\rho} \widetilde{u u'' v''}$ , is expected to be the primary contributor enhancing the surface heat flux, whereas the turbulent flux of enthalpy,  $c_p \bar{\rho} \widetilde{T'' v''}$ , naturally reduces the surface heat flux toward the wall because  $T_w \geq T_e$ , as is the case for most high-speed aerodynamic heating applications.

### 3. Streamwise growth of enthalpy thickness (III)

The contribution of the *streamwise growth* of the total enthalpy thickness to the surface heat flux originates from

$$\int_0^\infty (y - \ell) \frac{\partial}{\partial x} \left( \frac{\bar{\rho}}{\rho_e} \frac{\tilde{u}}{U_e} \left( \frac{H_e - \tilde{H}}{H_{\text{ref}} - H_w} \right) \right) dy = -\ell \frac{d\delta_H^\ell}{dx} + (\delta_H - \delta_H^\ell) \frac{d\ell}{dx}. \quad (34)$$

The total enthalpy thickness,  $\delta_H$ , from Eq. (21), represents the net streamwise flux of total enthalpy defect in the BL. The first moment of the total enthalpy defect flux is captured by  $\delta_H^\ell$ , the moment

of total enthalpy thickness. Equation (23) can be thought of as an equation for the growth rate of the moment of total enthalpy thickness,  $d\delta_H^\ell/dx$ , with all other terms being analogous to torques, redistributing the total enthalpy in the wall-normal direction to alter its moment about  $y = \ell(x)$ . Like the angular momentum thickness, the moment of total enthalpy thickness is a signed quantity; its rate of change with  $x$  can be positive or negative, depending on how it absorbs total enthalpy fluxes from the other terms. Moreover, the growth rate of moment of total enthalpy and angular momentum thicknesses are not necessarily the same due to the effect of Prandtl number and complex energy transfer mechanisms.

#### 4. Mean wall-normal flux (IV)

The *mean wall-normal* flux of total enthalpy is due to the wall-normal advection of total enthalpy deficit:

$$\int_0^\infty (y - \ell) \frac{\partial}{\partial y} \left( \frac{\bar{\rho}}{\rho_e} \tilde{v} \left( \frac{H_e - \tilde{H}}{H_{\text{ref}} - H_w} \right) \right) dy = -\delta_H^v. \quad (35)$$

This term represents how mean wall-normal velocity transports total enthalpy across the BL and affects the surface heat flux. It is analogous to the *mean wall-normal* torque in the AMI equation and will generally have the same behavior. A recent investigation of incompressible BLs revealed a negative contribution of *mean wall-normal* to the Stanton number because of the negative wall-normal velocity region in the vicinity of the surface during the transition to turbulence [51]. However, for a fully turbulent regime, the *mean wall-normal* flux is generally positive and weakly augments the surface heat flux.

#### 5. Nonzero edge pressure gradient and wall-temperature variation, (VI) and (VII)

Just as an adverse or favorable pressure gradient may act as torque to alter the mean velocity defect profile, the moment of total enthalpy thickness is also subject to edge pressure gradient effects. Additionally, any variation of the wall temperature also impacts the evolution of the moment of total enthalpy thickness. In this paper, ZPG BLs over isothermal walls are considered, so the exploration of these terms is left to future work.

#### 6. Departure from BL approximations (VIII)

All terms in total enthalpy conservation equation that are typically small in thin BLs are gathered in a single term, negligible fluxes. For high-speed BLs (with no BL separation), the *negligible terms* originate from the streamwise derivative of the streamwise heat flux,  $-\kappa \partial T / \partial x$ , and the streamwise velocity and total enthalpy covariance,  $\overline{\rho v'' \tilde{H}''}$ . While not relevant for the present paper, these terms could become significant and warrant more attention in flows such as incipient BL separation or shock-BL interactions.

## IV. COMPRESSIBLE TURBULENT BL DATA AND NUMERICAL METHODS

This section discusses the compressible turbulent BL data used to evaluate the AMI and MTEI equations, Eqs. (7) and (23), respectively. The data are obtained from DNSs of compressible BLs using a turbulent recycling method with zero edge pressure gradient [55]. A sixth-order hybrid scheme was utilized in the numerical simulations to ensure very low numerical dissipation. This scheme uses a skew-symmetric formulation [56] in smooth regions of the flow and a sixth-order targeted essentially nonoscillatory (TENO) scheme across discontinuities [57]. In low-Mach-number calculations, the TENO scheme is never utilized and the calculation is completely carried out using the skew-symmetric method. At higher Mach numbers, the TENO scheme is triggered only on a small fraction of the computational grid points. Since the Reynolds number is relatively high for the

TABLE III. DNS inputs and some fundamental flow outputs;  $Re_{\delta_{in}} = \rho_e U_e \delta_{in} / \mu_e$  is the Reynolds number based on the inflow BL thickness ( $\delta_{in}$ ); Prandtl number  $Pr = 0.72$ , (nondimensional) specific heat  $c_p = 3.5$ , and heat capacity ratio  $\gamma = 1.4$  are set as constants and the same for all cases.

Case		Inputs					Outputs						
ID	Color	$M_e$	$Re_{\delta_{in}}$	$\mu_w/\mu_e$	$T_w/T_{aw}$	$\rho_w/\rho_e$	$\rho_{min}/\rho_e$	$\rho_2/\rho_e$	$\rho_2/\rho_w$	$\mu_2/\mu_e$	$\mu_H/\mu_e$	$Re_2$	$Pe_H$
A-6		0.6	2800	1.05	1	0.94	0.94	0.98	1.04	1.03		294–959	
B-2		2	4736	1.49	1	0.58	0.58	0.80	1.38	1.34		299–928	
C-2		2	2800	1.02	0.6	0.96	0.85	0.90	0.93	1.09		244–816	
D-5		5	20 000	2.27	0.6	0.3	0.28	0.52	1.71	2.07	1.54	446–1238	681–1890
E-5		5	10 000	1.07	0.2	0.89	0.48	0.63	0.70	1.49	1.51	361–1104	388–1222
F-7		7	20 000	2.12	0.3	0.33	0.24	0.44	1.31	2.27	2.16	314–901	363–1079
G-7		7	10 000	1.63	0.2	0.49	0.28	0.47	0.95	2.07		182–571	

simulations, a second-order central finite-difference stencil is applied for the diffusion fluxes. The time integration is conducted using the strong-stability-preserving third-order Runge-Kutta method [58]. The system of equations for DNS is solved by the hypersonics task-based research solver [55].

The compressible fluid for DNS is air assumed as a perfect gas. The DNS data cover a range of edge Mach numbers,  $0.6 \leq M_e \leq 7$ , with different wall-temperature boundary conditions, including both cold walls and adiabatic walls. Table III lists the dimensionless input parameters in addition to parameters summarizing the variation of mean density and viscosity in the simulation results. The (Favre) average normalized velocity and Reynolds shear stress as a function of the wall-normal direction normalized by the semilocal length scale ( $y^*$ ) [59], are shown in Figs. 2(a) and 2(b), respectively. The average velocity profiles in Fig. 2(a) are normalized by  $U_e$ , reflecting their contributions to the integrands in the AMI equation. Figure 2(b) confirms that Reynolds shear stress profiles are similar near the wall when normalized by  $\tau_w$ . The peak of Reynolds shear stress does depend on the friction Reynolds number, which is not matched between each of the cases because of practical constraints.

Similar plots for the profiles of the (Favre) average total enthalpy and the total enthalpy and wall-normal velocity covariance are provided in Figs. 3(a) and 3(b). A subset of the simulations listed in Table III is included here to focus on the higher Mach number cases. Figure 3(a) exhibits

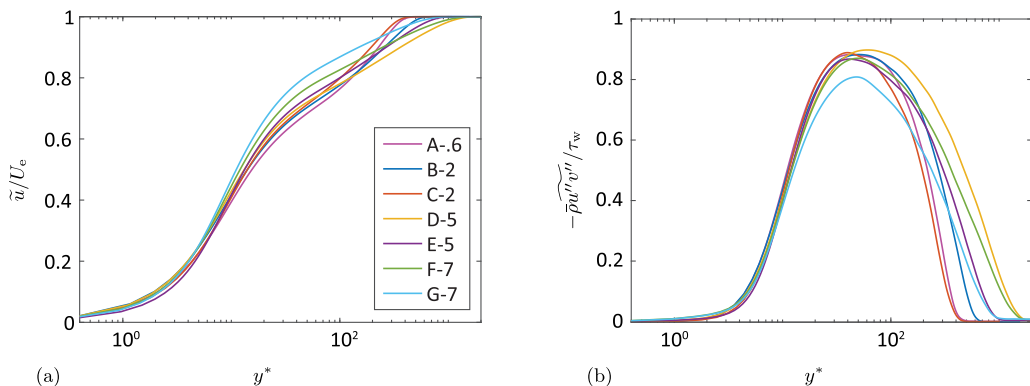


FIG. 2. Normalized Favre averaged (a) velocity by the edge velocity and (b) Reynolds shear stress by the wall shear stress. The profiles are plotted at  $Re_2$  shown with \* in Fig. 6(a).

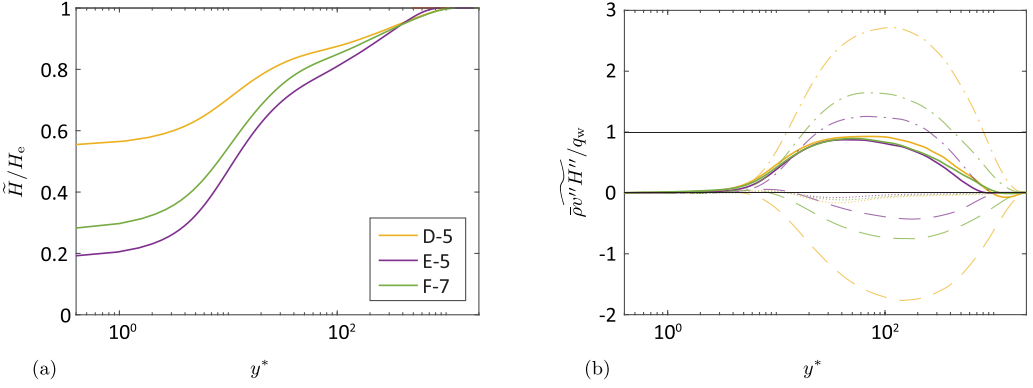


FIG. 3. Normalized Favre averaged (a) total enthalpy by the edge total enthalpy, and (b) wall-normal velocity and total enthalpy turbulent covariance by the wall heat flux (for study cases of MTEI equation). In (b) the dashed, dashed-dotted, and dotted lines represent  $c_p \overline{\rho T'' v''}$ ,  $\overline{\rho \tilde{u} u'' v''}$ , and  $\frac{1}{2} \overline{\rho u'' u'' v''}$ , respectively. The profiles are plotted at  $Pe_H$  shown with “\*” in Fig. 10(a).

the significance of Mach number and wall cooling on total enthalpy; stronger wall cooling generates a higher edge-wall total enthalpy difference, which is the primary potential of energy transfer within the BL. Figure 3(b) shows the turbulence covariance behaves similar to Reynolds shear stress profiles in Fig. 2(b), especially, close to the wall, when they are normalized by the surface heat flux,  $q_w$ . In addition, we decompose  $\overline{\rho v'' H''}$  to its major contributors according to Eq. (33), Fig. 3(b); the dashed lines represent the wall-normal turbulent flux of enthalpy ( $c_p \overline{\rho T'' v''}$ ), with negative impact on the net turbulent flux of total enthalpy,  $T_w \geq T_e$ , helping wall cooling. The dashed-dotted lines show the wall-normal turbulent transport of the mean kinetic energy,  $\overline{\rho \tilde{u} u'' v''}$ ; this transport mechanism enhances the net turbulent flux of total enthalpy by bringing the high energy eddies toward the wall where they stagnate, subsequently generate significant heating at the wall. Finally, the dotted lines represent the turbulent flux of turbulent kinetic energy,  $\frac{1}{2} \overline{\rho u'' u'' v''}$ , with relatively negative weak influence. The effect of compressibility on momentum and energy transport is due to the variation of density and viscosity within the BL. Density and viscosity are explicitly related to temperature; assuming perfect gas, since the pressure variation within the BL is small, density has a direct inverse relation with temperature. Moreover, viscosity is a function of temperature using Sutherlands’ law (with constants  $T_0 = 273.15$  K and  $S_0 = 110.4$  K) for air. In Figs. 4(a) and 4(b) the profiles of the average density and (Favre) average viscosity, respectively, are presented with respect to  $y^*$ . For cold-wall boundary conditions, the peak of temperature occurs within the BL, which coincides with minimum density and maximum viscosity; whereas for adiabatic wall boundary conditions, the temperature is maximum at the wall. Generally, higher  $M_e$  leads to lower density and higher viscosity, but the wall temperature also has a crucial effect on both density and viscosity within the BL. In Fig. 4(a), the dashed lines present the stress-weighted density expressed in Eq. (16). There is an inverse relation between edge Mach number and  $\rho_2$ ; the higher  $M_e$ , the lower  $\rho_2$ . In addition to the edge Mach number influence, higher wall temperature also decreases the stress-weighted density. This can be clearly observed by comparing D-5 and E-5, where  $\rho_2$  is smaller for D-5 with higher  $T_w$ .

Normalized  $\mu_2$  and  $\mu_H$ —reference viscosities in the AMI and MTEI equations—by the edge viscosity are shown in Fig. 4(b) with dashed and dashed-dotted lines, respectively. According to the definition of  $\mu_2$ , Eq. (11), the value of it is not necessarily between  $\mu_e$  and  $\mu_w$ , and it depends on the streamwise location. In fact,  $\mu_2$  absorbs the effect of wall cooling and the temperature rise within the BL. The deviation between  $\mu_2$  and  $\mu_H$  is smaller when the edge-wall temperature difference is weaker (strong wall cooling). For example, for E-5, which represents the highest wall-cooling case,

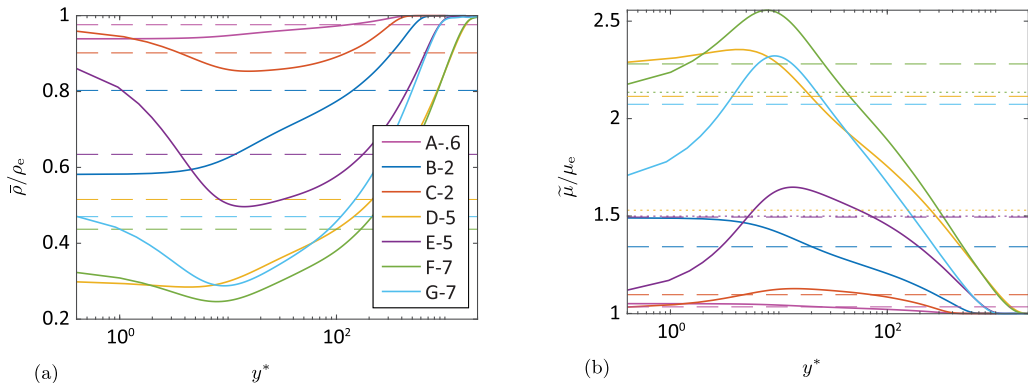


FIG. 4. Normalized (a) average density by the edge density and (b) Favre average viscosity by the edge viscosity. The dashed lines in (a) show  $\rho_2$ , Eq. (16). Also, the dashed and dotted lines in (b) represent the value of  $\mu_2$ , Eq. (11), and  $\mu_H$ , Eq. (28), respectively. The profiles are plotted at  $\text{Re}_2$  shown by \* in Fig. 6(a), except for  $\mu_H$  that is plotted at  $\text{Pe}_H$  shown by \* in Fig. 10(a).

the difference between  $\mu_2$  and  $\mu_H$  is about 1%. Conversely, this deviation becomes more substantial for the cases with higher  $T_w$ , like in D-5.

As discussed in Secs. II (for AMI equation) and III (for MTEI equation), to isolate the ZPG laminar contribution, it's necessary to determine the appropriate length scale  $\ell$ . This requires solving the self-similar momentum and energy equations for compressible (or incompressible) BLs. The Blasius solution can simply be used to get  $\ell$  according to an incompressible laminar BL. To obtain  $\ell$  from a compressible laminar BL, however, the system of self-similar ordinary differential equations (ODEs) is solved numerically by applying second-order finite-difference schemes and a Newton-Raphson method with a line-search algorithm [60]. The solver takes the required edge and wall flow parameters as inputs, provided in Table III, then outputs the self-similar velocity and temperature profiles. Using the self-similar solutions we compute the constants  $c_2$  (and  $c_H$ ) for the AMI (and MTEI) equation, which gives the suitable linear relationship between  $\ell$  and  $\delta_2$  (and  $\delta_H$ ) concerning the choice of the reference viscosity.

## V. RESULTS

So far, we derived the AMI and MTEI integral relations to decompose the skin friction and surface heat flux, respectively. Then, we introduced an approach to computing the appropriate length scale  $\ell$ , which isolates the ZPG laminar skin friction coefficient and Stanton number into a single term in the AMI and MTEI equations, respectively. Now, by choosing the reference viscosities and conductivities, we will apply the AMI and MTEI equations to the given DNS data discussed in Sec. IV.

### A. AMI analysis

This section exhibits the use of the AMI equation, Eq. (7), to analyze the DNS data sets summarized in Table III. For demonstration purposes, the stress-weighted viscosity,  $\mu_2$ , is chosen as the reference viscosity and the length scale is chosen proportional to the momentum thickness,  $\ell \sim \delta_2$ . The coefficient of proportionality is calculated from the ODE solution to the self-similar ZPG laminar BL equations described previously. Recall that the choice of  $\mu_2$  is motivated by the AMI equation, while the choice of  $\delta_2$  comes from its significance in the momentum integral equation; see Sec. II B. Thus, the following analysis interprets turbulent BL physics relative to

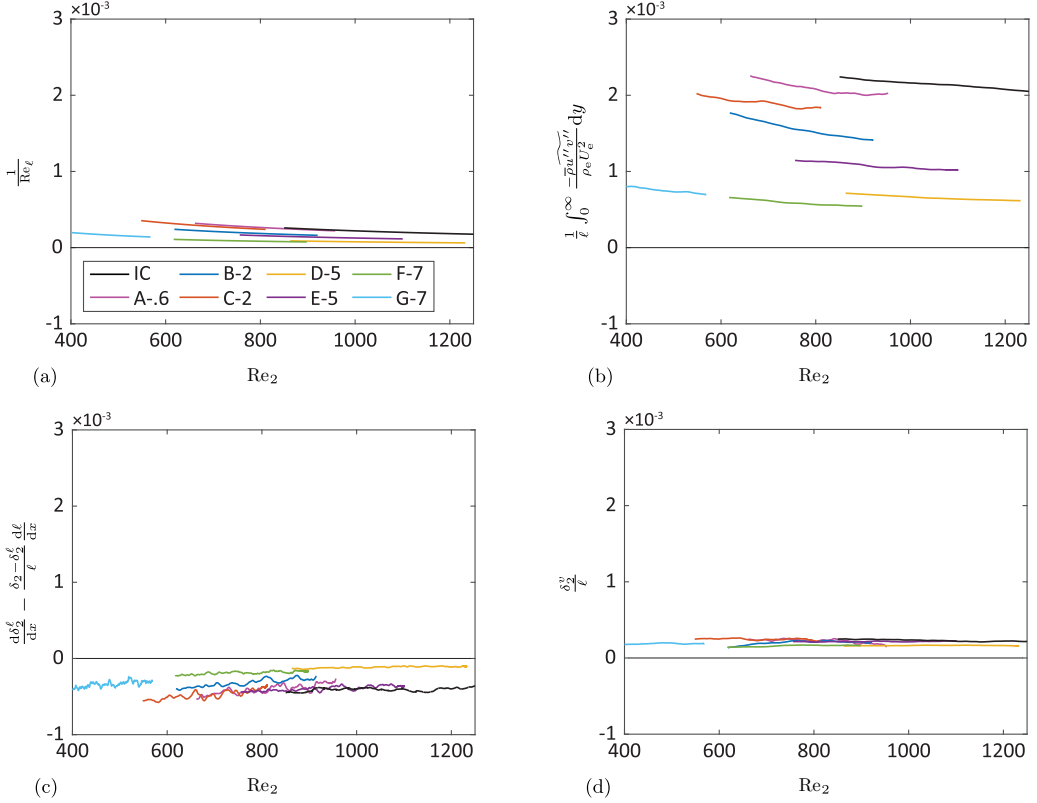


FIG. 5. Evaluation of non-negligible terms in the AMI equation, Eq. (7), based on  $\ell = \ell_{2,C}$  and  $\mu_{\text{ref}} = \mu_2$  for the cases in Table III within the fully turbulent regime: (a) baseline laminar skin friction, (b) the integral torque of the Reynolds shear stress, (c) the streamwise growth of the angular momentum thickness, and (d) the torque due to mean wall-normal velocity. Each term is shown as a function of  $\text{Re}_2$ , Eq. (14). A part of the upstream data is truncated because of the effect of the turbulent recycling.

a baseline laminar BL having the same edge Mach number ( $M_e$ ), edge temperature ( $T_e$ ), wall temperature ( $T_w$ ), and the Reynolds number defined by  $\text{Re}_2 = \rho_e U_e \delta_2 / \mu_2$ .

With this choice, the AMI length scale is based on a compressible laminar solution is  $\ell = \ell_{2,C}$ , where the subscripts 2 and C denote the reference viscosity,  $\mu_2$ , and compressible laminar solution, respectively. Another related possibility, which is a useful foil, is to use an incompressible laminar BL, i.e., a solution to the Blasius equation [44], as the baseline for AMI analysis. This laminar BL is still chosen to match the  $\text{Re}_2$  of the turbulent BL to be analyzed, but the edge Mach number is zero and no temperature variation is included,  $T_w = T_e$ . This choice is denoted  $\ell = \ell_{1C}$  where IC signifies the choice of an incompressible laminar BL.

Figure 5 presents each term in the AMI equation using  $\text{Re}_2$  and  $\ell_{2,C}$ . Data from an incompressible (IC) turbulent BL simulation with heat transfer [51,61] are also included. For the given data, the maximum (streamwise averaged) relative residual error of the AMI equation, Eq. (7), is less than or (approximately) equal to 5%. The residual error in closing the AMI equation from DNS data is primarily caused by statistical convergence error, which is amplified by the streamwise derivative needed to compute the term proportional to  $d\delta_2^\ell/dx$ . Thus, the error depends mostly on the length of time used for averaging each simulation and the error for the cases shown here was deemed sufficiently small for our present purposes.

Figure 5(a) presents the  $C_f/2$  of the equivalent compressible ZPG laminar BL at the same Reynolds number,  $\text{Re}_2$ . The laminar skin friction is relatively small compared to the fully turbulent

BL—about 15%—and diminishes slowly with the Reynolds number,  $\sim \text{Re}_2^{-1}$ . The reference laminar BL depends on  $M_e$ ,  $T_e$ , and  $T_w$  of the turbulent BL case, so this term shows some variation as expected, though not significant compared with the *turbulent torque*, Fig. 5(b). The integral of the Reynolds shear stress is the primary contributor to enhancing  $C_f/2$  compared with the other terms. It represents the total torque due to Reynolds shear stress carrying high-momentum flow toward the wall. This behavior is consistent with the observation in Ref. [53] (for  $M_e = 2.5$  and the adiabatic wall, using edge viscosity for the reference Reynolds number). The *turbulent torque* gradually diminishes with  $\text{Re}_2$  approximately at the same pace as  $C_f/2$ .

In Fig. 5(c), the rate of the *streamwise growth* of the angular momentum thickness is shown for each case. This term has a negative contribution to the skin friction, as the turbulent BL grows thicker than its laminar counterpart, absorbing a small part of the Reynolds shear stress torque into the growth of the angular momentum. According to Fig. 5(c), the variation in this term is substantially less than that of the Reynolds shear stress integral in Fig. 5(b). Nonetheless, a minor opposite trend can be observed.

The contribution of the *mean wall-normal torque* to  $C_f/2$  is presented in Fig. 5(d). For a fully turbulent regime, the *mean wall-normal torque* has a relatively weak influence and does not vary significantly with streamwise direction, consistent with previous observations of incompressible flows [50,51]. It worth mentioning the other terms on the right-hand side of AMI equation, including *edge pressure gradient torque* and *negligible terms*, are at least order of magnitude smaller than those shown here. Also, the *deviation* term vanishes when  $\mu_{\text{ref}} = \mu_2$  by definition. For completeness, these terms are shown in Appendix B.

The impact of the edge Mach number and wall temperature on the terms in the AMI equation is succinctly demonstrated in Fig. 5, showing a greater influence by the edge Mach number than the wall temperature. The viscous dissipation roughly scales with  $M_e^2$  and generates high temperatures in the near-wall region. As the pressure remains approximately uniform across the BL, the density in the near-wall region decreases with increasing Mach number. The ability of correlated velocity fluctuations,  $u''v''$ , to cause a net momentum flux is proportional to the mean density,  $\bar{\rho}$ . Therefore, the *turbulent torque* in the AMI equation generally decreases with increasing  $M_e$ . The *laminar* and *streamwise growth* terms similarly depend on the mean density and decrease in magnitude with increasing  $M_e$ . The variation in *turbulent torque* is clearly the dominant effect in Fig. 5 so the skin friction decreases with increasing  $M_e$ . This is consistent with the well-known inverse relationship between the edge Mach number and the skin-friction coefficient for laminar and turbulent BLs [12,62].

After the effect of the edge Mach number, the AMI equation is also sensitive to the wall temperature. Lower wall temperatures (stronger wall cooling) are known to increase the laminar and turbulent skin frictions [62,63]. Higher wall temperature enhances the turbulent wall-normal transport of the Reynolds shear stress away from the wall [64]. Thus, when the surface temperature is higher, lower skin friction drag is expected. Figure 5 shows that the enhancement of *turbulent torque* by lower  $T_w$  is significant. For example, comparing D-5 and E-5 with the same  $M_e = 5$  but one with strong wall cooling (E-5) shows roughly 20% higher *turbulent torque* for E-5. A similar trend can also be seen for  $M_e = 2$  by comparing B-2 and C-2. The difference in wall temperature for F-7 and G-7 ( $T_w/T_{\text{aw}} = 0.3$  and  $0.2$ , respectively) is apparently not large enough to cause a noticeable difference in the AMI terms. As with Mach number, the increase of Reynolds shear stress with decreasing wall temperature can be linked to an associated increase in the near-wall mean density. Generally, increase in *turbulent torque* due to lower wall temperatures is slightly offset by a much weaker opposing trend in the *streamwise growth* of angular momentum.

In Fig. 6, we directly consider the skin friction coefficient (the sum of terms shown in Fig. 5) and further investigate the impact of the edge Mach number and wall temperature on the *turbulent torque*. Figure 6(a) compares the skin friction with the sum of the right-hand terms in the AMI equation, verifying the calculations. Also shown is the *turbulent torque*, which is just one of the terms in the AMI equation. Evidently, the trend in turbulent torque closely matches the skin friction

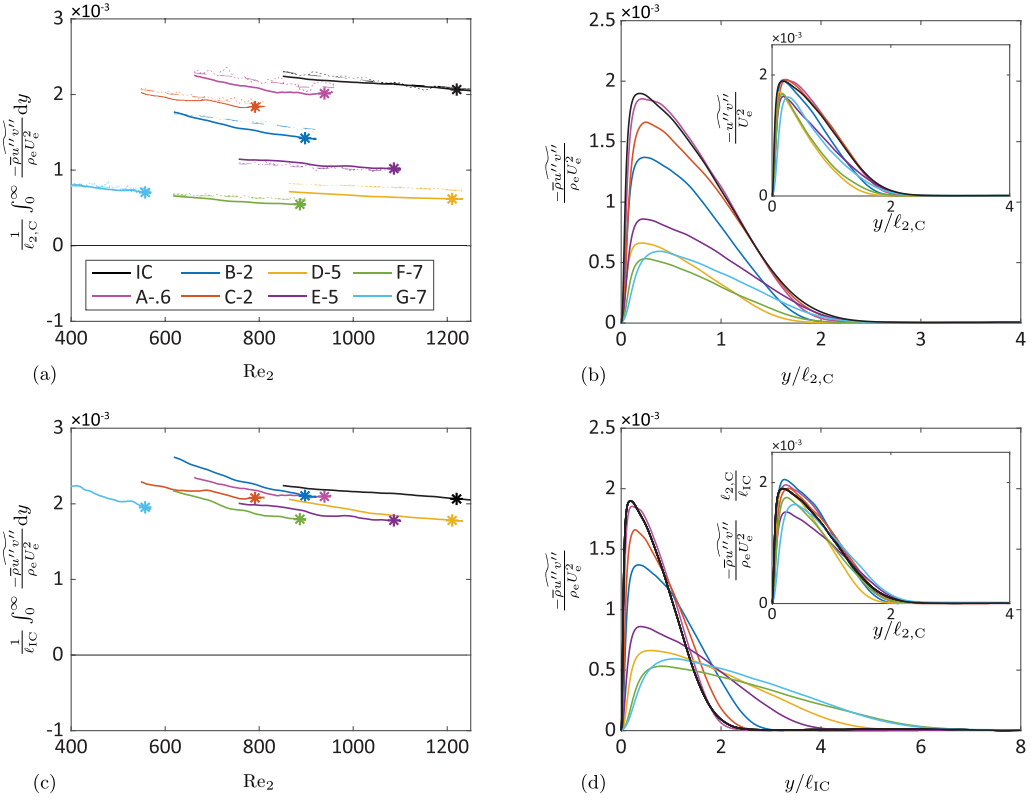


FIG. 6. Contribution of the *turbulent torque* to  $C_f/2$  and the profile of its integrand at \*: (a) turbulent torque by choosing  $\ell$  based on self-similar laminar compressible BLs,  $\ell = \ell_{2,C}$ , and (b) profile of the integrand of turbulent torque with respect to wall-normal distance normalized by  $\ell_{2,C}$ . In (a), the thinner dashed and dotted lines show the  $C_f/2$  and the right-hand side of the AMI equation. The Inset of (b) exhibits the integrand of turbulent torque by removing the effect of density variation within the BL. (c) The *turbulent torque* by choosing  $\ell$  based on Blasius solution for IC BLs,  $\ell = \ell_{1C}$ , and (d) profile of the integrand of the *turbulent torque* with respect to the wall-normal distance normalized by  $\ell_{1C}$ . Inset of (d) presents the integrand of the *turbulent torque* multiplied by the ratio of compressible and incompressible length scales,  $\ell_{2,C} = \ell_{1C}$ , with respect to  $y/\ell_{2,C}$ .

coefficient trend with  $M_e$  and  $T_w$ . To examine this in more detail, Fig. 6(b) compares the integrand of the *turbulent torque* term. Interestingly, the length scale  $\ell_{C,2}$  is fairly effective in collapsing the wall-normal extent of the turbulent BLs across different Mach numbers and wall temperatures. The trend in skin friction coefficient, then, can be traced to the variation in the magnitude of the Reynolds shear stress,  $-\overline{\rho u'' v''}$ . To quantify the extent to which the trends in Reynolds shear stress magnitude may be explained by the trends in near-wall mean density discussed in the previous two paragraphs, the inset of Fig. 6(b) shows the Reynolds shear stress profiles divided by the mean density. The result is a significant increase in similarity amongst the cases, even if there is not complete collapse. Therefore, the effect of  $M_e$  and  $T_w$  on the skin friction coefficient may be mostly explained by the influence of mean density,  $\rho$ , in determining the efficiency with which correlated velocity fluctuations,  $\widetilde{u'' v''}$ , transport momentum across the BL. More specifically, at higher edge Mach number (and/or higher wall temperature), lower near-wall density reduces the momentum transport, and subsequently skin friction.

Alternatively, the variation of skin-friction coefficient with  $M_e$  and  $T_w$  may be tied to trends in the laminar compressible BL. Figure 6(c) shows the *turbulent torque* from the AMI equation when the

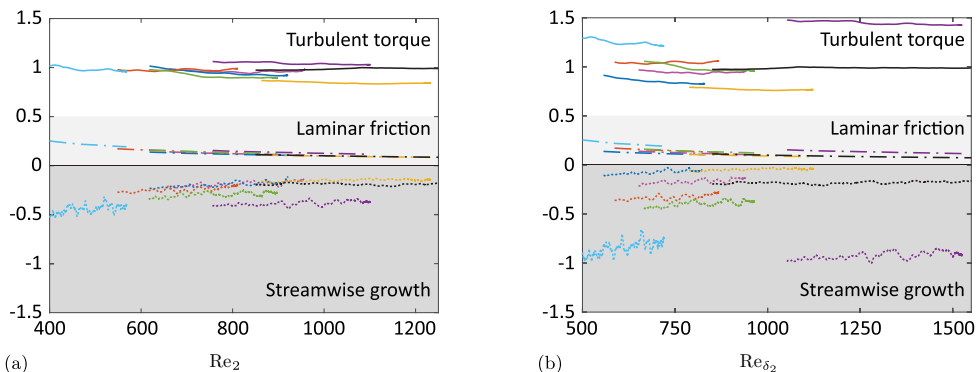


FIG. 7. Normalized contribution of *turbulent torque* (white background), *laminar friction* (light gray background), and *streamwise growth* (dark gray background) by  $C_f/2$ : when the reference viscosity (a)  $\mu_{\text{ref}} = \mu_2$ , and (b)  $\mu_{\text{ref}} = \mu_w$ . In (b),  $Re_{\delta_2} = U_e \rho_e \delta_2 / \mu_w$  is the Reynolds number based on the wall viscosity.

baseline laminar BL is chosen at  $M_e = 0$  rather than at the matching  $M_e$  of the turbulent case. In other words,  $\ell = \ell_{\text{IC}}$  is the same for all cases, calculated using the solution to the Blasius equation. Interestingly,  $\ell_{\text{IC}}$  leads to much closer collapse for the *turbulent torque* compared with the compressible length scale  $\ell_{2,C}$  (matched  $M_e$ ) in Fig. 6(a). However, there is still some variation in Fig. 6(c) and the Reynolds shear stress profiles, i.e., the integrands of the *turbulent torque*, show substantial differences in Fig. 6(d). Both the width ( $y/\ell$  axis) and peak are different for each case, showing a strong dependence on  $M_e$  and  $T_w$ , though the integrals of each curve are quite similar. According to Fig. 6(b), as already seen for higher  $M_e$ , the peak of the profile of the normalized Reynolds shear stress is lower, yet the width related to  $\ell_{\text{IC}}$  is larger. For example, the width of integrands for F-7 and G-7 extend beyond  $y/\ell_{\text{IC}} = 6$ . Also, colder wall temperature causes stronger maximum normalized Reynolds shear stress but over a smaller relative width. This can be seen by comparing the profiles of D-5 with E-5, or B-2 with C-2. Inset of Figure 6(d) shows the normalized Reynolds shear stress by the edge conditions multiplied by the ratio between the compressible and incompressible length scales,  $\ell_{2,C}/\ell_{\text{IC}}$ , plotted with respect to  $y/\ell_{2,C}$  [consistent with Fig. 6(b)]. Although there is still a subtle edge Mach number influence, in the inset of Fig. 6(d), there is a better collapse between the cases with the same  $T_w/T_{\text{aw}}$  ratio –representation of wall-cooling strength. For instance, comparing C-2 and D-5,  $T_w/T_{\text{aw}} = 0.6$ , we observe the peak values are roughly the same (but slightly shifted). Therefore, the skin friction of a high-speed turbulent BL relative to a  $M_e = 0$  turbulent BL may be quantitatively (but not perfectly) tied to the same relative comparison for laminar BLs, provided the comparisons are done at matched  $Re_2$  as defined in Eq. (14).

In the analysis of turbulent BLs, it is common to use the viscosity at the wall,  $\mu_w$ , as the reference viscosity. This has proven particularly effective when the wall temperature is near the adiabatic wall temperature [65]. In Fig. 7, we study the comparison between choosing  $\mu_{\text{ref}} = \mu_2$  and  $\mu_{\text{ref}} = \mu_w$  on *turbulent torque* (white background), *laminar friction* (light gray background), and *streamwise growth* (dark gray background). In this figure, each term from the right-hand side of the AMI equation, Eq. (7), is normalized by  $C_f/2$ . Thus, this figure can be interpreted as showing the percent contribution of each term to the skin friction coefficient.

For  $\mu_{\text{ref}} = \mu_2$  in Fig. 7(a), the normalized *turbulent torque* is almost equal to one for both cases, which is consistent with the dominant effect of turbulence on momentum transport and skin friction enhancement. This is simply another way to visualize the data from Fig. 6(a), where it was already shown that the *turbulent torque* term closely followed the skin friction coefficient for  $\ell = \ell_{2,C}$ . Choosing  $\mu_2$  as the reference viscosity leads to a closer collapse of the *turbulent torque* around one (1.0) for the given data compared with the result of choosing the wall viscosity as the reference, Fig. 7(b). This can be clearly seen for E-5 (purple) which has the strongest wall cooling, and the normalized *turbulent torque* is roughly 50% larger. A similar effect is observed for the *laminar*

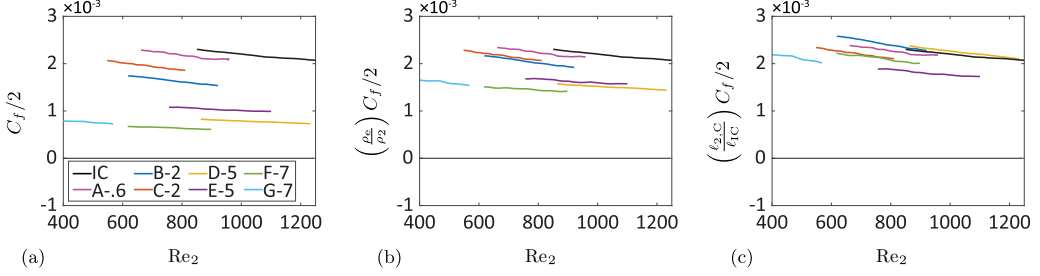


FIG. 8. (a) Skin friction coefficients without transformation, (b) integral transformation based on stress-weighted density, and (c) integral transformation based on the ratio of the compressible and incompressible AMI length scales.

friction and *streamwise growth* when  $\mu_{\text{ref}} = \mu_w$ . In fact, taking E-5 as an example again, we observe almost 300% higher negative contribution by normalized *streamwise growth* if we pick  $\mu_w$  as the reference viscosity. The effect of the wall temperature is much weaker when choosing  $\mu_{\text{ref}} = \mu_2$ . This comparison provides a further justification for the use of  $\mu_2$ —as the reference viscosity—in the above analysis, in addition to its physical interpretability as the stress-weighted average viscosity. This choice enables the identification of some of the above trends with mean density and laminar BL length scale.

The overall impact of the trends observed in Figs. 6 and 7 can be concisely summarized in terms of the overall impact on skin friction by using the trends to construct transformations between compressible and incompressible skin friction coefficient. Figure 8 shows the results of two such transformations: (i) based on stress-weighted density,  $\rho_2$ , and (ii) laminar BL length scale,  $\ell$ .

Figure 8(a) shows  $C_f/2$  for the compressible and incompressible data without transformation. Assuming  $C_f/2$  is roughly equal to the *turbulent torque*, combined with the role of mean density observed in Fig. 6(b), suggests multiplying  $C_f/2$  with the ratio of  $\rho_e/\rho_2$ . According to Fig. 8(b), this transformation only partially compensates for different edge Mach numbers and wall temperature; it is not a strong enough correction to compensate for the entirety of the compressibility effect. Indeed, a closer inspection of Fig. 6(b) indicates that the peak of  $u''v''/U_e^2$  still varies noticeably for  $M_e = 5$  and 7. Thus, the AMI equation provides a way to quantify the impact of lower mean density on the skin friction coefficient. The density ratio correction  $\rho_e/\rho_2$  is too simple to explain the entire effect of compressibility but still explains a significant part of it. There are several explanations of this including the effect of the imposed boundary conditions, e.g., viscosity variation, and internal regulation that becomes considerable for relatively high  $M_e$  [66,67].

Another transformation approach is inspired by Fig. 6(c) where the Blasius solution was used to obtain the AMI length scale,  $\ell = \ell_{IC}$ , and a relatively suggestive collapse of *turbulent torques* was observed. Figure 6(d) further shows the ability of the length scale ratio between compressible and incompressible laminar flows,  $\ell_{2,C}/\ell_{IC}$ , in obtaining better similarity in the Reynolds shear stress profiles. Because for a fully turbulent regime, the dominant source of skin friction is due to Reynolds shear stress, we apply this ratio of length scales directly to the skin friction in Fig. 8(c). This transformation performs well for the adiabatic wall cases with about a maximum deviation of 4% from the incompressible  $C_f/2$ . However, strong wall cooling still creates noticeable deviation for  $(\ell_{2,C}/\ell_{IC})C_f/2$  from the incompressible  $C_f/2$ , up to roughly 20% for E-5. Thus, the self-similar laminar BL solutions appear useful in providing information about turbulent BL skin friction, at least when the stress-weighted average viscosity is used to define the Reynolds number,  $Re_2$ , at which the relevant ratios are computed.

## B. MTEI analysis

At high Mach numbers, the surface heat transfer is often of greater concern than the skin friction drag. Therefore, quantitative mapping of flow phenomena throughout the BL and how they alter

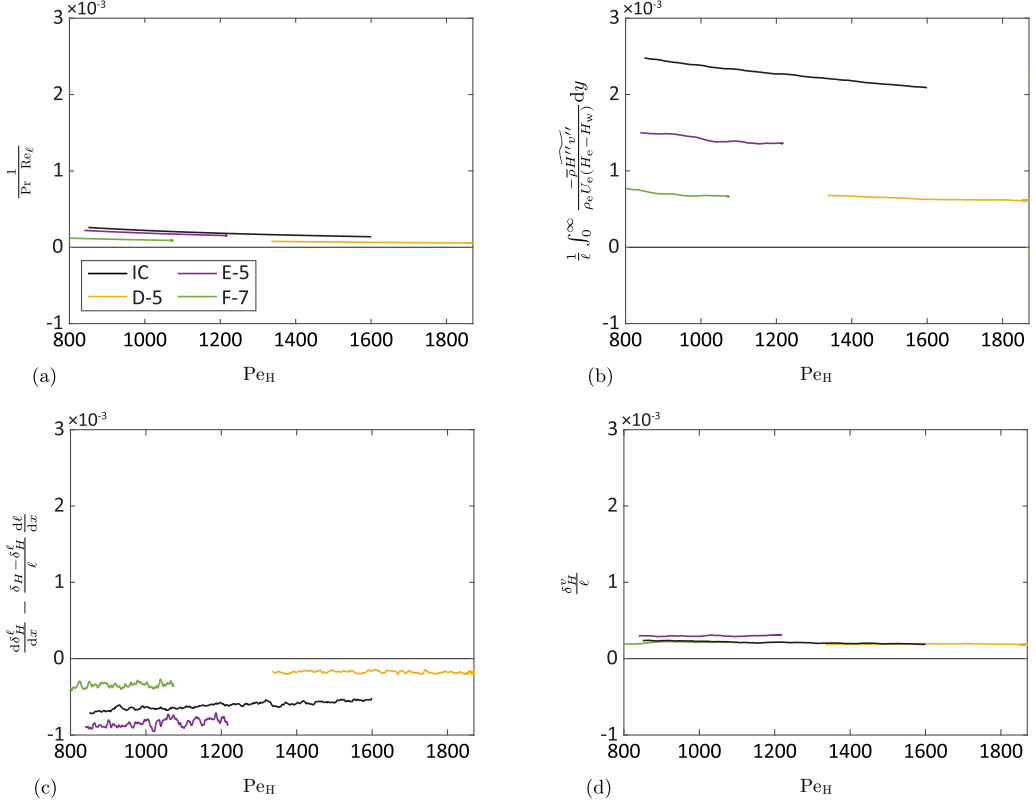


FIG. 9. Budget of MTEI based on  $\ell = \ell_{H,C}$  and  $\mu_{\text{ref}} = \mu_H$  within the fully turbulent regime: (a) laminar Stanton number, (b) contribution of turbulent flux to Stanton number, (c) streamwise growth of the first moment of total enthalpy thickness, and (d) contribution of mean wall-normal flux. The incompressible (IC) data are shown in black. A part of the upstream data is truncated because of the effect of the turbulent recycling.

the Stanton number is crucial. In this section, we apply the MTEI analysis, discussed in Sec. III, to the DNS data with relatively high edge Mach numbers and nonzero surface heat flux. We limit our focus to the higher Mach number cases D-5, E-5, and F-7 for which the wall temperature is lower than the adiabatic wall temperature but higher than the edge wall temperature. G-7 is not included in the MTEI analysis as it is quite similar to F-7—the same edge Mach number and very close wall-cooling effect—but with lower Reynolds number range. This similar behavior was already observed in the AMI analysis, Sec. V A, especially in Fig. 5(b) in which the turbulence skin friction enhancement of F-7 is approximately the continuation of G-7 at higher Reynolds number. The compressible data are compared with the incompressible, constant property turbulent BL with heat transfer [61]. For the incompressible BL data, the nondimensional wall-edge temperature difference and Prandtl number are unity. Most of the discussion provided in Sec. II for the AMI equation and momentum transport is analogous to the MTEI equation and energy transport, but a bit more complex. The total enthalpy conservation is the basis of the MTEI equation, which consists of two energy transport mechanisms: kinetic energy and internal energy. Considering the Mach number as a dimensionless ratio of kinetic energy and internal energy, for incompressible flows the kinetic is neglected,  $M_e = 0$ . Conversely, for high-speed flows, the kinetic energy is significant and even dominant.

Figure 9 shows the breakdown of the Stanton number using the MTEI equation for the four major flow phenomena (the full budget is provided in Appendix C) with respect to the Peclet number  $Pe_H = Re_H Pr_{\text{ref}}$ , where  $Re_H = \rho_e \delta_H U_e / \mu_H$  is the Reynolds number based on the given reference

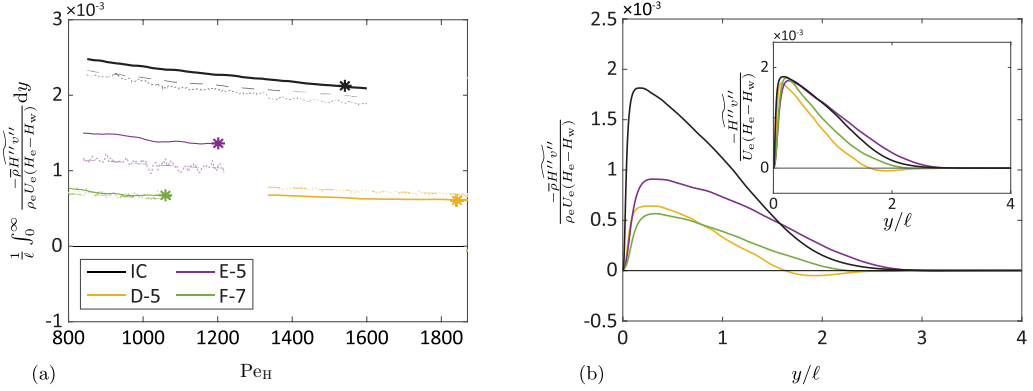


FIG. 10. Contribution of *turbulent flux* to St and the profile of its integrand at \*: (a) turbulent flux of total enthalpy based on  $\ell = \ell_{H,C}$  and (b) profile of its integrand with respect to the wall-normal distance normalized by  $\ell_{H,C}$ . In (a), the dim thin dashed and dotted lines show the St and the right-hand side of the MTEI equation. The inset of (b) shows the integrand of *turbulent flux* by pulling out the influence of density variation within the BL.

viscosity. (Recall that  $Pr_{ref} = 1$  is chosen here to make the St number based on the edge stagnation temperature rather than the adiabatic wall temperature.) Here the length scale  $\ell = \ell_{H,C}$  is determined based on the reference viscosity  $\mu_{ref} = \mu_H$  and self-similar ZPG compressible laminar BL solution. Figure 9(a) shows the *laminar* Stanton number that gradually diminishes with the Peclet number,  $Pe_H$ , as we go further downstream. According to Figs. 9(a) and 9(d), the *mean wall-normal* transport also weakly contributes to the surface heat flux and does not show a significant variation between the cases. Moreover, similar to its AMI counterpart, the *mean wall-normal* change with respect to  $Pe_H$  is negligible.

Figure 9(b) exhibits the direct contribution of turbulence on surface heat flux through wall-normal turbulent flux of total enthalpy,  $-\overline{\rho H'' v''}$ . The *turbulent flux* is larger in magnitude and shows more significant variation than the other three terms shown in Fig. 9. Since both kinetic and internal energies are embedded within the definition of total enthalpy, the contribution of the *turbulent flux* of total enthalpy to the Stanton number in the MTEI equation can be split; according to Fig. 3(b), the turbulent transport of the mean kinetic energy,  $\overline{\rho u'' v''}$ , is the primary contributor due to relatively high  $Me$  (high edge kinetic energy). Turbulence via Reynolds shear stress carries this kinetic energy flow toward the wall where it stagnates and generates a tremendous amount of heat flux toward the wall. Conversely, the turbulent flux of enthalpy,  $c_p \overline{\rho T'' v''}$ , partially removes high internal energy flows from the wall toward the edge ( $T_w \geq T_{we}$ ). In other words, the balance of these two mechanisms is essentially the net contribution of *turbulent flux* to the Stanton number.

The *streamwise growth* of the first moment of total enthalpy thickness is the only negative term. In fact, *streamwise growth* helps cooling the wall by absorbing some of the turbulent flux into downstream growth rather than wall heat flux. For instance, comparing D-5 and E-5, it is evident the flux by *streamwise growth* is more substantial for E-5 with more intense wall cooling.

In Fig. 4(a), the significant reduction of the near-wall mean density due to the rise of temperature within the BL was shown. This reduction, subsequently, decreases the turbulent momentum and total enthalpy flux. According to Fig. 10(a), the ratio of *turbulent flux* and the Stanton number is roughly between 90% to over 130%. This number is closer to  $\approx 90\%$  for D-5 (weakest wall cooling). However, the *turbulent flux* becomes greater than the Stanton number for the cases with stronger wall cooling, such as E-5. The enhancement of *turbulent flux* for the cases with strong wall cooling is examined in Fig. 10(b); here, we plot the profile of its integrand with respect to the wall-normal direction within the fully turbulent regime, at \*. Evidently, there is no meaningful similarity in the profiles of the integrands. However, by removing the mean density variation

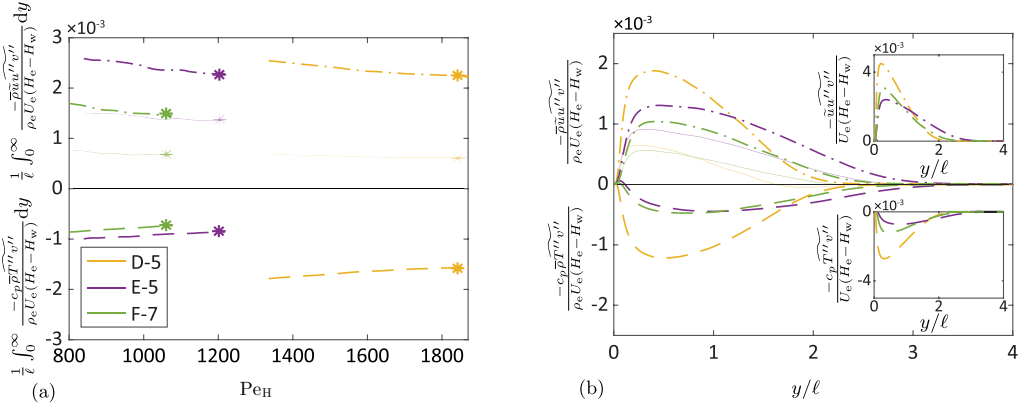


FIG. 11. Decomposition of the *turbulent flux* of total enthalpy and the profile of its integrand at \*: (a) direct contribution of turbulent transport of mean kinetic energy (dashed-dotted line) and turbulent enthalpy (heat) flux (dashed lines) to  $St$  with respect to the streamwise location,  $Pe_H$ , and (b) profile of their integrands with respect to wall-normal distance normalized by  $\ell_{H,C}$ . In (a), (b), the dim thin solid lines represent the net contribution of the turbulent flux of total enthalpy. Insets of (b) show the integrands by pulling out the effect of density variation within the BL.

across the BL, inset of Fig. 10(b), the profiles become significantly more similar, even if they do not truly collapse. In other words, much of the variation in *turbulent flux* contributions to the enhanced surface heat flux can be attributed simply to the lower mean density in the near-wall region diminishing the effectiveness of turbulent fluctuations in transporting energy toward the wall. In fact, by removing the effect of density variation across the BL, the contribution of *turbulent flux* to  $St$ , for all cases, are significantly more similar to the incompressible case. This observation matches the results observed earlier in the inset of Fig. 6(b) for the *turbulent torque* by the Reynolds shear stress.

In Fig. 10, the turbulent flux of total enthalpy is consistently higher for the strongly cooled case E-5. To shed more light on this, Fig. 11 explores the decomposition of the total enthalpy flux,  $\overline{\rho v'' H''}$ , into two components: (i) the turbulent transport of mean kinetic energy,  $\overline{\rho u'' v''}$ , and (ii) the turbulent enthalpy flux,  $c_p \overline{\rho T'' v''}$ . Figure 11(a) represents their direct contribution to  $St$ . The Reynolds shear stress increases  $St$  by bringing the mean kinetic energy toward the wall. On the other hand, the turbulent enthalpy flux advects enthalpy away from the wall for most of the BL (except below the temperature peak). The profiles of the integrands of turbulent transport of mean kinetic energy and turbulent enthalpy flux in Fig. 11(b) confirms the aforementioned effect; the profile of turbulent enthalpy flux for F-7 is just slightly lower than E-5, yet there is a clear drop in the turbulent transport of mean kinetic energy for F-7 with a higher edge Mach number. In contrast to the influence of  $Me$ , which was more effective on turbulent flux of mean kinetic energy, the impact of  $T_w$  is more substantial on turbulent enthalpy flux rather than turbulent transport of mean kinetic energy. According to Fig. 11(a), a comparison between D-5 and E-5 reveals stronger wall cooling in E-5 slightly (about 10%) reduces the turbulent transport of mean kinetic energy flux. On the other hand, the (absolute) effect of turbulent flux of enthalpy drops substantially for roughly 80%. The weaker effect of turbulent enthalpy flux in case E-5 may be conceptually associated with a smaller temperature difference,  $T_w - T_e$ , due to stronger wall cooling.

Despite the relative similarity observed for the total enthalpy flux in the inset of Fig. 10(b) after removing the density effect, the two contributing fluxes (turbulent enthalpy flux and turbulent flux of the mean kinetic energy) individually do not show the same degree of similarity in Fig. 11(b). Here, by removing the explicit influence of density variation on turbulent fluxes, the effect of the edge Mach number is significantly reduced, so the profiles are then sorted primarily based on the imposed

wall temperature from the highest, D-5, to the lowest, E-5; higher  $T_w$  leads to larger integrand magnitudes.

Taking D-5 as an example with the hottest wall in the given DNS data justifies the concept of the heat conduction due to the edge-wall temperature difference and how turbulent enthalpy flux toward the edge resist the generated heat at the wall by stagnating edge kinetic energy. In fact, this mechanism explains the net negative  $\overline{\rho v'' H''}$  values close to the edge of BL from  $y/\ell \approx 1.7$  to  $y/\ell \approx 2.3$ , where turbulent enthalpy flux (negative contribution to net St) becomes greater than the turbulent transport of the mean kinetic energy (positive contribution to net St). In conclusion, the turbulent transport of the total enthalpy via mean kinetic energy is slightly more localized near the wall and attenuates lightly quicker away from the wall rather than the turbulent enthalpy flux.

In summary, this section shows the capability of the MTEI equation as a quantitative mapping between the flow phenomena above the wall and how they impact the net surface heat flux. Using the MTEI, we can distinguish the contribution of kinetic energy and internal energy on heat flux, and we can understand how and when they resist each other depending on the given edge and wall flow conditions.

## VI. CONCLUSION

In this paper, an AMI equation is introduced for compressible flow BLs with variable density and viscosity. The AMI equation was introduced in previous work for incompressible BLs [50]. The AMI equation provides a simple way to quantify how turbulence and other flow phenomena impact the BL skin friction coefficient relative to an equivalent ZPG laminar BL. Moreover, a MTEI equation is developed for high-speed BLs with surface heat flux. Analogous to the AMI equation, the MTEI equation quantifies the enhancement of a BL's Stanton number by turbulent fluxes and other flow phenomena relative to the laminar BL case. The resulting AMI and MTEI equations are given in Eqs. (7) and (23), respectively. A calorically perfect gas assumption is maintained in this paper but can be relaxed to include high-enthalpy effects in future works.

The AMI equation is an integral conservation law for the first moment about  $y = \ell(x)$  of velocity defect, normalized to be written in terms of the skin-friction coefficient. The length scale,  $\ell$ , about which the moment is taken to be the center of action of the viscous force for a laminar BL sharing the same Reynolds number, such that the skin friction of an equivalent ZPG laminar BL is isolated into a single term as a function of the Reynolds number only. This choice allows the other terms in the AMI equation to be straightforwardly interpreted as an enhancement (or attenuation) of skin friction coefficient relative to the laminar baseline case. The length scale for the Reynolds number similarity can be tailored to suit the desired interpretation of the analysis.

Similarly, the MTEI equation is an integral conservation law for the first moment of total enthalpy defect, written in the dimensionless form in terms of the Stanton number. For the MTEI equation, the moment is centered about the center of action of the combined conductive heat flux and viscous kinetic energy flux for an equivalent ZPG laminar BL. This results in an equation that contains the laminar BL Stanton number in a single term as a function of the Reynolds (or Peclet) number, allowing a specific interpretation of the other terms in the MTEI equation as enhancements or attenuations of surface heat flux relative to the baseline laminar case.

For compressible BLs with variable viscosity, a reference viscosity must also be chosen. The form of the AMI equation itself suggests the choice of the shear stress weighted viscosity,  $\mu_2$ , as the representative viscosity of the BL. Moreover, a reference viscosity and conductivity,  $\mu_H$  and  $\kappa_H$ , respectively, emerge from the MTEI equation as natural choices for representative transport coefficients in high-speed BLs.

The compressible AMI equation was applied to the DNS data from turbulent BLs having a range of edge Mach numbers,  $M_e$ , and wall-temperature boundary conditions,  $T_w$ . Relative to laminar BLs

with the same  $M_e$ ,  $T_w$ , and momentum thickness Reynolds number based on  $\mu_2$  ( $Re_2$ ), the trend in skin friction for turbulent BLs closely followed the behavior in the Reynolds shear stress integral. It is demonstrated that choosing  $\mu_2$  shows a better collapse for compressible BLs compared with the choice of  $\mu_w$ .

A closer inspection of the Reynolds shear stress integrand revealed that the lower skin friction for higher  $M_e$ , higher  $T_w$  cases is associated primarily with lower near-wall mean densities. The effect of compressibility on skin-friction coefficient may be summarized as follows. Fluid entrained into the BL from the edge is decelerated with tiny pressure variations across the BL, leading to higher temperatures and lower densities in the near-wall region. Turbulent enhancement of wall shear stress relies primarily on the transport of momentum across the BL by the Reynolds shear stress,  $-\overline{\rho u'' v''}$ . Normalized by the edge velocity,  $U_e^2$ , the covariance of streamwise and wall-normal velocities does not vary as strongly with  $M_e$  and  $T_w$ . However, the mean density drops significantly in the near-wall region for high  $M_e$  and  $T_w$ , significantly decreasing the turbulent momentum flux, leading to lower skin-friction coefficients.

An alternative description of skin friction coefficient trends in compressible BLs can be made using the incompressible laminar solution (i.e., Blasius). The ratio of length scales based on the incompressible and compressible laminar solutions is shown to also capture much of the variation in skin friction coefficient with  $M_e$  and  $T_w$ . This suggests that, when BLs are compared with similarity based on  $Re_2 = \rho_e U_e \delta_2 / \mu_2$ , the effect of compressibility on laminar BLs somewhat closely matches its impacts on turbulent BLs, especially for adiabatic or weakly cooled walls.

Applying the MTEI equation to the DNS data set with nonzero heat flux, an analogous compressibility effect was observed for the total enthalpy transport. Reduction in the Stanton number observed at higher edge Mach numbers and wall temperatures could be most explained by simply considering the impact of mean density on turbulent fluxes. However, another physical effect relating to wall cooling,  $T_w - T_e$  (edge-wall temperature difference), was observed. The lower the edge-wall temperature difference in the case of strongly cooled walls suppresses the turbulent enthalpy flux ( $c_p \overline{\rho v'' T''}$ ) much more than the turbulent transport of the mean kinetic energy ( $\overline{\rho u'' v''}$ ). In fact, this further explores how intense wall cooling breaks the analogy between the skin-friction coefficient and Stanton number.

In conclusion, the AMI and MTEI equations are shown to be a practical tool for using DNS (or experimental) data to elucidate essential physics in high-speed turbulent BLs. The present paper demonstrates their use for fully turbulent BLs with a calorically perfect gas. One possible future approach is to further quantify the contribution of different turbulent length scales (turbulent structures) using the AMI and MTEI equations. This will be fruitful to comprehend the effect of turbulent structures in compressible BLs on surface drag and heat transfer in comparison with incompressible BLs. It would also facilitate the exploration of how the integral approach, pursued here, may complement existing velocity profile transformations to elucidate high-speed effects on turbulent BL physics. Crucial applications to hypersonic aerothermodynamics can be addressed with extensions of AMI and MTEI to include high-enthalpy effects such as variable specific heats because of the vibrational excitation and changing chemical composition. The peak surface heat flux during transition to turbulence is often crucial, so the application of the MTEI equation to transitional BLs with various instability modes may prove quite fruitful, given the exceptional trends that have been observed using moment-integral equations for transitional incompressible BLs [50,51]. Ultimately, this line of research can provide a robust, more quantitative understanding of the relationship between transitional and turbulent flow physics and the dangerously high surface heat fluxes on hypersonic vehicles.

#### ACKNOWLEDGMENTS

This work was completed in part during the Summer Program of the Center for Turbulence Research at Stanford University. A.E. acknowledges support from NASA under Grant No.

80NSSC20M0201. C.W. acknowledges support by the National Science Foundation Graduate Research Fellowship Program under Grant No. DGE-2146755.

### APPENDIX A: STEP-BY-STEP FULL DERIVATION OF ANGULAR MOMENTUM INTEGRAL EQUATION

Here the step-by-step derivation of the AMI equation is provided. Favre average Navier-Stokes equation for statistically two-dimensional compressible BLs reads

$$\frac{\partial \bar{\rho}}{\partial t} + \frac{\partial}{\partial x}(\bar{\rho} \tilde{u}) + \frac{\partial}{\partial y}(\bar{\rho} \tilde{v}) = 0 \quad (\text{A1})$$

for continuity, and

$$\frac{\partial}{\partial t}(\bar{\rho} \tilde{u}) + \frac{\partial}{\partial x}(\bar{\rho} \tilde{u} \tilde{u}) + \frac{\partial}{\partial y}(\bar{\rho} \tilde{u} \tilde{v}) = -\frac{d\bar{p}}{dx} + \frac{\partial}{\partial x}(\overline{\tau_{xx}} - \bar{\rho} \tilde{u}'' \tilde{u}'') + \frac{\partial}{\partial y}(\overline{\tau_{xy}} - \bar{\rho} \tilde{u}'' \tilde{v}'') \quad (\text{A2})$$

for  $x$  momentum, where we assumed the mean pressure is not changing in  $y$  direction. We further can assume

$$\overline{\tau_{xy}} \approx \mu \overline{\frac{\partial u}{\partial y}}. \quad (\text{A3})$$

The governing equation at the edge of the BL yields

$$\frac{\partial}{\partial t}(\rho_e U_e) + \rho_e U_e \frac{dU_e}{dx} = -\frac{dP_e}{dx}, \quad (\text{A4})$$

presuming the edge conditions are independent of the wall-normal direction,  $y$ . Subtracting Eq. (A2) from Eq. (A4) gives the average  $x$ -momentum deficit equation as

$$\rho_e U_e \frac{dU_e}{dx} - \frac{\partial}{\partial x}(\bar{\rho} \tilde{u} \tilde{u}) - \frac{\partial}{\partial y}(\bar{\rho} \tilde{u} \tilde{v}) = -\frac{\partial}{\partial y} \left( \overline{\mu \frac{\partial u}{\partial y}} \right) + \frac{\partial}{\partial y}(\bar{\rho} \tilde{u}'' \tilde{v}'') - I_2, \quad (\text{A5})$$

in which

$$I_2 = \frac{\partial}{\partial t}(\rho_e U_e - \bar{\rho} \tilde{u}) + \frac{\partial}{\partial x} \left( -\bar{\rho}(\tilde{u}'' \tilde{u}'') + \frac{\partial}{\partial x}(\overline{\tau_{xx}}) \right) - \left( \frac{dP_e}{dx} - \frac{d\bar{p}}{dx} \right), \quad (\text{A6})$$

representing the negligible terms for statistically two-dimensional BLs. Rearranging Eq. (A5) and implementing the continuity equation, the  $x$ -momentum deficit can be rewritten as

$$\begin{aligned} & \rho_e U_e \frac{dU_e}{dx} \left( \left( 1 - \frac{\bar{\rho} \tilde{u}}{\rho_e U_e} \right) + 2 \left( \frac{\bar{\rho} \tilde{u}}{\rho_e U_e} \left( 1 - \frac{\tilde{u}}{U_e} \right) \right) \right) + U_e^2 \frac{d\rho_e}{dx} \left( \frac{\bar{\rho} \tilde{u}}{\rho_e U_e} \left( 1 - \frac{\tilde{u}}{U_e} \right) \right) \\ & + \rho_e U_e^2 \frac{\partial}{\partial x} \left( \frac{\bar{\rho} \tilde{u}}{\rho_e U_e} \left( 1 - \frac{\tilde{u}}{U_e} \right) \right) + \rho_e U_e^2 \frac{\partial}{\partial y} \left( \frac{\bar{\rho} \tilde{v}}{\rho_e U_e} \left( 1 - \frac{\tilde{u}}{U_e} \right) \right) \\ & + \frac{\partial}{\partial y} \left( \overline{\mu \frac{\partial u}{\partial y}} \right) - \frac{\partial}{\partial y}(\bar{\rho} \tilde{u}'' \tilde{v}'') + I_2 = 0. \end{aligned} \quad (\text{A7})$$

To obtain the angular momentum (or the first moment of momentum) form, we multiply the whole Eq. (A7) by  $(y - \ell)$ , where  $\ell = \ell$  is the appropriate choice of length scale based on laminar skin friction discussed in Sec. II. Then, we integrate the equation in the wall-normal direction,  $\int_0^\infty (y -$

$\ell(x))\{ \cdot \} dy = 0$ . Integration of the first two terms on the left-hand side of Eq. (A7) yields

$$\begin{aligned} (1) &\rightarrow \rho_e U_e \frac{dU_e}{dx} \int_0^\infty (y - \ell) \left\{ \left( 1 - \frac{\bar{\rho}}{\rho_e} \frac{\tilde{u}}{U_e} \right) + 2 \left( \frac{\bar{\rho}}{\rho_e} \frac{\tilde{u}}{U_e} \left( 1 - \frac{\tilde{u}}{U_e} \right) \right) \right\} dy \\ &= -\ell \rho_e U_e \frac{dU_e}{dx} \int_0^\infty \left( 1 - \frac{y}{\ell} \right) \left\{ \left( 1 - \frac{\bar{\rho}}{\rho_e} \frac{\tilde{u}}{U_e} \right) + 2 \left( \frac{\bar{\rho}}{\rho_e} \frac{\tilde{u}}{U_e} \left( 1 - \frac{\tilde{u}}{U_e} \right) \right) \right\} dy \\ &= -\ell \rho_e U_e \frac{dU_e}{dx} (\delta_1^\ell + 2\delta_2^\ell), \end{aligned}$$

$$\begin{aligned} (2) &\rightarrow U_e^2 \frac{d\rho_e}{dx} \int_0^\infty (y - \ell) \left\{ \frac{\bar{\rho}}{\rho_e} \frac{\tilde{u}}{U_e} \left( 1 - \frac{\tilde{u}}{U_e} \right) \right\} dy = -\ell U_e^2 \frac{d\rho_e}{dx} \int_0^\infty \left( 1 - \frac{y}{\ell} \right) \left\{ \frac{\bar{\rho}}{\rho_e} \frac{\tilde{u}}{U_e} \left( 1 - \frac{\tilde{u}}{U_e} \right) \right\} dy \\ &= -U_e^2 \frac{d\rho_e}{dx} \delta_2^\ell. \end{aligned}$$

These two terms originate from the edge pressure gradient due to the streamwise variation of edge velocity and density, respectively. The integration of the third term in the left-hand side of Eq. (A7), which represents the streamwise variation of the streamwise flux of momentum deficit, gives

$$\begin{aligned} (3) &\rightarrow \rho_e U_e^2 \int_0^\infty (y - \ell) \left\{ \frac{\partial}{\partial x} \left( \frac{\bar{\rho}}{\rho_e} \frac{\tilde{u}}{U_e} \left( 1 - \frac{\tilde{u}}{U_e} \right) \right) \right\} dy \\ &= -\ell \rho_e U_e^2 \left( \frac{\partial}{\partial x} \int_0^\infty \left( 1 - \frac{y}{\ell} \right) \left\{ \frac{\bar{\rho}}{\rho_e} \frac{\tilde{u}}{U_e} \left( 1 - \frac{\tilde{u}}{U_e} \right) \right\} dy \right. \\ &\quad \left. + \frac{1}{\ell} \frac{d\ell}{dx} \left( - \int_0^\infty \left( 1 - \frac{y}{\ell} \right) \left\{ \frac{\bar{\rho}}{\rho_e} \frac{\tilde{u}}{U_e} \left( 1 - \frac{\tilde{u}}{U_e} \right) \right\} dy + \int_0^\infty \frac{\bar{\rho}}{\rho_e} \frac{\tilde{u}}{U_e} \left( 1 - \frac{\tilde{u}}{U_e} \right) dy \right) \right) \\ &= -\ell \rho_e U_e^2 \left( \frac{d\delta_2^\ell}{dx} + \frac{\delta_2^\ell - \delta_2}{\ell} \frac{d\ell}{dx} \right). \end{aligned}$$

The fourth term in Eq. (A7) depends on the mean wall-normal flux of the streamwise momentum deficit. Integration of this term and applying no penetration through the wall reads

$$\begin{aligned} (4) &\rightarrow \rho_e U_e^2 \int_0^\infty (y - \ell) \frac{\partial}{\partial y} \left\{ \frac{\bar{\rho}}{\rho_e} \frac{\tilde{v}}{U_e} \left( 1 - \frac{\tilde{u}}{U_e} \right) \right\} dy \\ &= -\ell \rho_e U_e^2 \left( \left[ \left( 1 - \frac{y}{\ell} \right) \frac{\bar{\rho}}{\rho_e} \frac{\tilde{v}}{U_e} \left( 1 - \frac{\tilde{u}}{U_e} \right) \right]_0^\infty + \frac{1}{\ell} \int_0^\infty \frac{\bar{\rho}}{\rho_e} \frac{\tilde{v}}{U_e} \left( 1 - \frac{\tilde{u}}{U_e} \right) dy \right) = -\rho_e U_e^2 \delta_2^v. \end{aligned}$$

The viscous effect and wall shear stress is embedded in the fifth term on the left-hand side of Eq. (A7). Integrating this term across the wall-normal direction gives

$$\begin{aligned} (5) &\rightarrow \int_0^\infty (y - \ell) \left\{ \frac{\partial}{\partial y} \left( \overline{\mu \frac{\partial u}{\partial y}} \right) \right\} dy = \left[ (y - \ell) \left( \overline{\mu \frac{\partial u}{\partial y}} \right) \right]_0^\infty - \int_0^\infty \overline{\mu \frac{\partial u}{\partial y}} dy \\ &= \ell \tau_w - \int_0^\infty (\overline{\mu} - \mu_{\text{ref}}) \frac{\partial u}{\partial y} dy - \mu_{\text{ref}} U_e. \end{aligned}$$

Integration of the sixth term yields

$$\begin{aligned} (6) &\rightarrow \int_0^\infty (y - \ell) \left\{ -\frac{\partial}{\partial y} (\overline{\rho u'' v''}) \right\} dy = - \left[ (y - \ell) \frac{\partial}{\partial y} (\overline{\rho u'' v''}) \right]_0^\infty + \int_0^\infty \overline{\rho u'' v''} dy \\ &= \int_0^\infty \overline{\rho u'' v''} dy, \end{aligned}$$

where the contribution of Reynolds shear stress on skin friction is preserved. It's worth mentioning that the integral of the Reynolds shear stress—without using the first moment method—vanishes

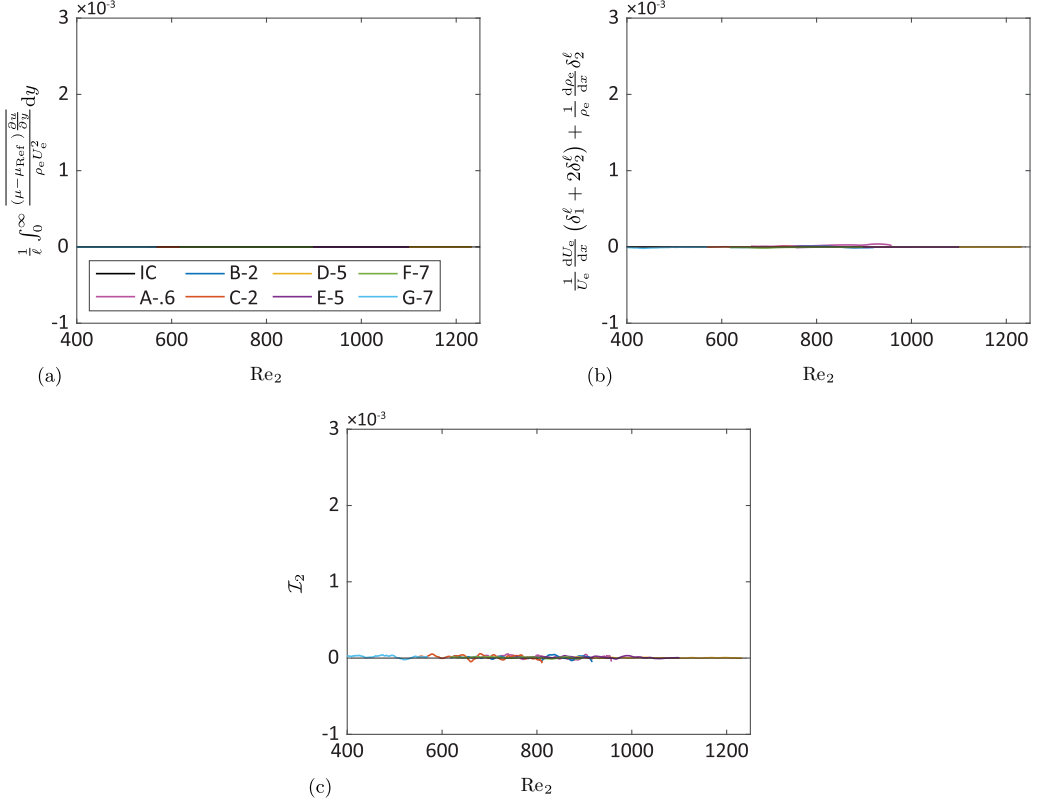


FIG. 12. Contribution of (a) viscous deviation from reference viscosity, (b) torque due to the edge pressure gradient, and (c) the negligible terms due to departure from the BL approximations to the AMI equation, Eq. (7), based on  $\mu_{\text{ref}} = \mu_2$  and  $\ell = \ell_{2,C}$ .

because the turbulence doesn't naturally exist at the wall nor within the irrotational edge. Finally, the integral of the seventh term which represents all the negligible flow phenomena for statistically two-dimensional BLs is

$$(7) \rightarrow \int_0^\infty (y - \ell) \{I_2\} dy = \ell \int_0^\infty \left(1 - \frac{y}{\ell}\right) \{I_2\} dy.$$

Normalizing all the integrals determined above with the edge dynamic pressure,  $\rho_e U_e / 2$ , yields the AMI equation for skin-friction coefficient  $C_f$ :

$$\begin{aligned} \frac{C_f}{2} = & \frac{1}{Re_\ell} + \frac{1}{\ell} \int_0^\infty \frac{-\bar{\rho} \widetilde{u'' v''}}{\rho_e U_e^2} dy + \left\{ \frac{d\delta_2^\ell}{dx} - \frac{\delta_2 - \delta_2^\ell}{\ell} \frac{d\ell}{dx} \right\} + \frac{\delta_2^v}{\ell} + \frac{1}{\ell} \int_0^\infty \frac{(\mu - \mu_{\text{ref}}) \frac{\partial u}{\partial y}}{\rho_e U_e^2} dy \\ & + \left\{ \frac{1}{U_e} \frac{dU_e}{dx} (\delta_1^\ell + 2\delta_2^\ell) + \frac{1}{\rho_e} \frac{d\rho_e}{dx} \delta_2^\ell \right\} + \mathcal{I}_2^\ell. \end{aligned} \quad (\text{A8})$$

In the above equation,

$$\mathcal{I}_2^\ell = \frac{1}{\rho_e U_e^2} \int_0^\infty \left(1 - \frac{y}{\ell}\right) I_2 dy \quad (\text{A9})$$

is the contribution of all negligible terms to skin-friction coefficient.

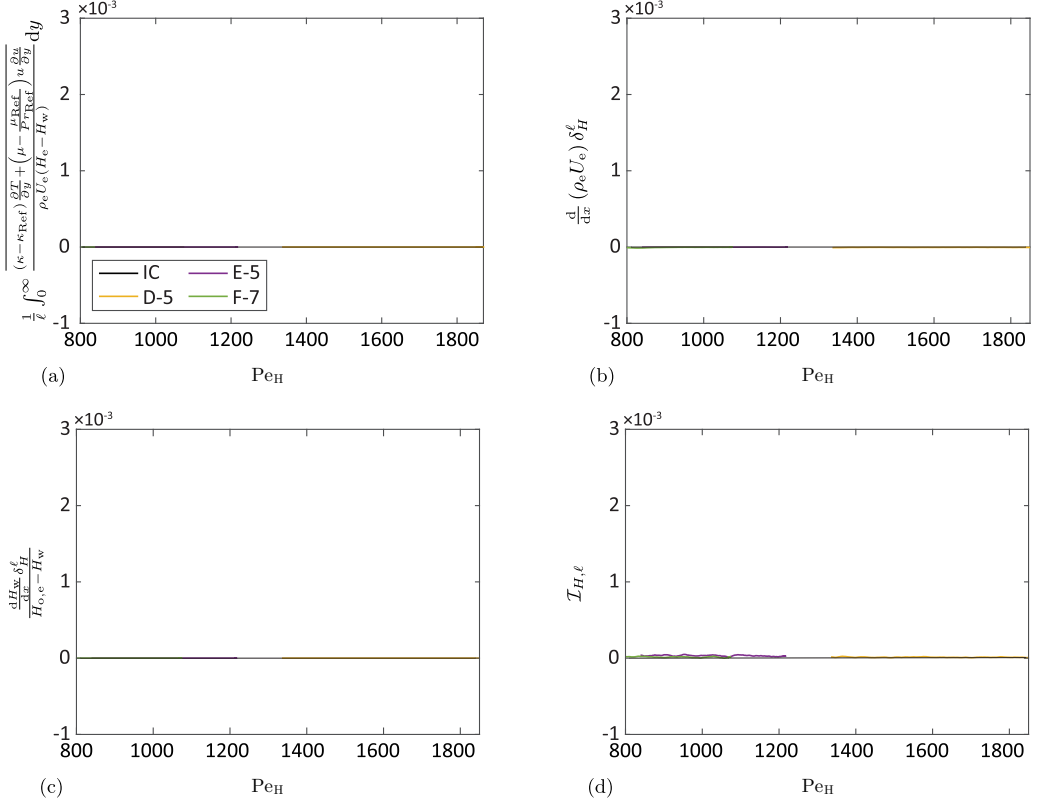


FIG. 13. Contribution of (a) deviation from reference viscous transport, (b) flux due to the edge pressure gradient, (c) nonisothermal wall temperature, and (d) the negligible terms due to departure from the BL approximations to the MTEI equation, Eq. (23), based on  $\mu_{\text{ref}} = \mu_H$  and  $\ell = \ell_{H,C}$ .

Deriving the MTEI equation, Eq. (23), takes similar steps elaborated above, but starting with the total enthalpy equation for compressible BLs.

#### APPENDIX B: FULL BUDGET OF ANGULAR MOMENTUM INTEGRAL EQUATION

In Figs. 5(a)–5(d), the four major terms in the AMI equation with choosing the shear stress weighted viscosity as the reference viscosity,  $\mu_{\text{ref}} = \mu_2$ , and self-similar compressible laminar solution as the base for the AMI length scale,  $\ell = \ell_{2,C}$ , are shown. Here, the contributions of the other flow phenomena are provided to complete the budget of the AMI equation. Figure 12(a) exhibits the *deviation* from reference viscosity which is equal to (machine) zero for all cases due to the choice of  $\mu_2$ . Figures 12(b) and 12(c) show the *edge pressure gradient torque* and negligible terms due to BL approximations, respectively. As expected, the contribution of these three flow phenomena are substantially weaker than the major ones in Fig. 5.

#### APPENDIX C: FULL BUDGET OF MOMENT OF TOTAL ENTHALPY INTEGRAL EQUATION

To complete the budget of the MTEI equation, here we provide the contribution of the other flow phenomena, including the flux due to *deviation* from reference viscous transport, *edge pressure gradient flux*, *negligible terms*, and *wall temperature variation* flux to the surface heat transfer. Similar to Figs. 9(a)–9(d), the reference viscosity is  $\mu_H$  and the MTEI length scale is computed from the self-similar compressible laminar solution,  $\ell = \ell_{H,C}$ . Figure 13(a) represents the flux of

total enthalpy due to the deviation from the reference viscous transport which is naturally equal to (machine) zero by the choice of  $\mu_{\text{ref}} = \mu_H$ . The contribution of nonzero edge pressure gradient on surface heat flux is also substantially small since the DNS data are for the zero edge pressure gradient, Fig. 13(b). Similarly, the influence of *negligible* terms and *wall temperature variation* on surface heat flux are substantially small since the DNS data are for zero edge pressure gradient and isothermal wall, respectively.

- 
- [1] S. K. Robinson, Coherent motions in the turbulent boundary layer, [Annu. Rev. Fluid Mech. \*\*23\*\*, 601 \(1991\)](#).
  - [2] G. V. Candler, Rate effects in hypersonic flows, [Annu. Rev. Fluid Mech. \*\*51\*\*, 379 \(2019\)](#).
  - [3] I. A. Leyva, The relentless pursuit of hypersonic flight, [Phys. Today \*\*70\*\*\(11\), 30 \(2017\)](#).
  - [4] M. V. Morkovin, Effects of compressibility on turbulent flows, [Colloq. Int. Mec. Turbul. \*\*367\*\*, 26 \(1962\)](#).
  - [5] E. F. Spina and A. J. Smits, Organized structures in a compressible, turbulent boundary layer, [J. Fluid Mech. \*\*182\*\*, 85 \(1987\)](#).
  - [6] S. J. Kline, W. C. Reynolds, F. A. Schraub, and P. W. Runstadler, The structure of turbulent boundary layers, [J. Fluid Mech. \*\*30\*\*, 741 \(1967\)](#).
  - [7] J. Kim, P. Moin, and R. Moser, Turbulence statistics in fully developed channel flow at low Reynolds number, [J. Fluid Mech. \*\*177\*\*, 133 \(1987\)](#).
  - [8] J. Jiménez and P. Moin, The minimal flow unit in near-wall turbulence, [J. Fluid Mech. \*\*225\*\*, 213 \(1991\)](#).
  - [9] J. Jiménez and A. PINELLI, The autonomous cycle of near-wall turbulence, [J. Fluid Mech. \*\*389\*\*, 335 \(1999\)](#).
  - [10] I. Marusic and J. P. Monty, Attached Eddy model of wall turbulence, [Annu. Rev. Fluid Mech. \*\*51\*\*, 49 \(2019\)](#).
  - [11] A. Townsend, *The Structure of Turbulent Shear Flow*, Cambridge Monographs on Mechanics (Cambridge University Press, 1976).
  - [12] F. M. White and J. Majdalani, *Viscous Fluid Flow*, Vol. 3 (McGraw-Hill, New York, 2006).
  - [13] E. R. Van Driest, Turbulent boundary layer in compressible fluids, [J. Aeronaut. Sci. \*\*18\*\*, 145 \(1951\)](#).
  - [14] P. G. Huang, G. N. Coleman, and P. Bradshaw, Compressible turbulent channel flows: DNS results and modelling, [J. Fluid Mech. \*\*305\*\*, 185 \(1995\)](#).
  - [15] G. N. Coleman, J. Kim, and R. D. Moser, A numerical study of turbulent supersonic isothermal-wall channel flow, [J. Fluid Mech. \*\*305\*\*, 159 \(1995\)](#).
  - [16] Y.-S. Zhang, W.-T. Bi, F. Hussain, X.-L. Li, and Z.-S. She, Mach-Number-Invariant Mean-Velocity Profile of Compressible Turbulent Boundary Layers, [Phys. Rev. Lett. \*\*109\*\*, 054502 \(2012\)](#).
  - [17] A. Trettel and J. Larsson, Mean velocity scaling for compressible wall turbulence with heat transfer, [Phys. Fluids \*\*28\*\*, 026102 \(2016\)](#).
  - [18] P. S. Volpiani, P. S. Iyer, S. Pirozzoli, and J. Larsson, Data-driven compressibility transformation for turbulent wall layers, [Phys. Rev. Fluids \*\*5\*\*, 052602\(R\) \(2020\)](#).
  - [19] K. P. Griffin, L. Fu, and P. Moin, Velocity transformation for compressible wall-bounded turbulent flows with and without heat transfer, [Proc. Natl. Acad. Sci. USA \*\*118\*\*, e2111144118 \(2021\)](#).
  - [20] H. Lee, P. Martin, and O. Williams, Compressible boundary layer velocity transformation based on a generalized form of the total stress, [arXiv:2112.13818 \[physics.flu-dyn\]](#).
  - [21] A. J. Smits, B. J. McKeon, and I. Marusic, High-Reynolds number wall turbulence, [Annu. Rev. Fluid Mech. \*\*43\*\*, 353 \(2011\)](#).
  - [22] N. Hutchins and I. Marusic, Evidence of very long meandering features in the logarithmic region of turbulent boundary layers, [J. Fluid Mech. \*\*579\*\*, 1 \(2007\)](#).
  - [23] N. Hutchins and I. Marusic, Large-scale influences in near-wall turbulence, [Philos. Trans. R. Soc. A \*\*365\*\*, 647 \(2007\)](#).
  - [24] B. Ganapathisubramani, N. Clemens, and D. Dolling, Large-scale motions in a supersonic turbulent boundary layer, [J. Fluid Mech. \*\*556\*\*, 271 \(2006\)](#).

- [25] D. B. De Graaff and J. K. Eaton, Reynolds-number scaling of the flat-plate turbulent boundary layer, *J. Fluid Mech.* **422**, 319 (2000).
- [26] I. Marusic and G. J. Kunkel, Streamwise turbulence intensity formulation for flat-plate boundary layers, *Phys. Fluids* **15**, 2461 (2003).
- [27] R. Mathis, N. Hutchins, and I. Marusic, A predictive inner-outer model for streamwise turbulence statistics in wall-bounded flows, *J. Fluid Mech.* **681**, 537 (2011).
- [28] I. Marusic, R. Mathis, and N. Hutchins, Predictive model for wall-bounded turbulent flow, *Science* **329**, 193 (2010).
- [29] M. M. Metzger and J. C. Klewicki, A comparative study of near-wall turbulence in high and low Reynolds number boundary layers, *Phys. Fluids* **13**, 692 (2001).
- [30] J. Lee and T. Zaki, Signature of large-scale motions on turbulent/non-turbulent interface in boundary layers, *J. Fluid Mech.* **819**, 165 (2017).
- [31] H. Choi, P. Moin, and J. Kim, Active turbulence control for drag reduction in wall-bounded flows, *J. Fluid Mech.* **262**, 75 (1994).
- [32] Y. Chang, S. S. Collis, and S. Ramakrishnan, Viscous effects in control of near-wall turbulence, *Phys. Fluids* **14**, 4069 (2002).
- [33] S. Deck, N. Renard, R. Laraufie, and P.-É. Weiss, Large-scale contribution to mean wall shear stress in high-Reynolds-number flat-plate boundary layers up to 13650, *J. Fluid Mech.* **743**, 202 (2014).
- [34] M. de Giovanetti, Y. Hwang, and H. Choi, Skin-friction generation by attached eddies in turbulent channel flow, *J. Fluid Mech.* **808**, 511 (2016).
- [35] K. Fukagata, K. Iwamoto, and N. Kasagi, Contribution of Reynolds stress distribution to the skin friction in wall-bounded flows, *Phys. Fluids* **14**, L73 (2002).
- [36] A. Bannier, É. Garnier, and P. Sagaut, Riblet Flow model based on an extended FIK identity, *Flow, Turbul. Combust.* **95**, 351 (2015).
- [37] J. Kim, Physics and control of wall turbulence for drag reduction, *Philos. Trans. R. Soc. A* **369**, 1396 (2011).
- [38] Y. Peet and P. Sagaut, Theoretical prediction of turbulent skin friction on geometrically complex surfaces, *Phys. Fluids* **21**, 105105 (2009).
- [39] F. Mehdi and C. M. White, Integral form of the skin friction coefficient suitable for experimental data, *Exp. Fluids* **50**, 43 (2011).
- [40] F. Mehdi, T. G. Johansson, C. M. White, and J. W. Naughton, On determining wall shear stress in spatially developing two-dimensional wall-bounded flows, *Exp. Fluids* **55**, 1 (2014).
- [41] Q.-J. Xia, W.-X. Huang, C.-X. Xu, and G.-X. Cui, Direct numerical simulation of spatially developing turbulent boundary layers with opposition control, *Fluid Dyn. Res.* **47**, 025503 (2015).
- [42] C. Wenzel, T. Gibis, and M. Kloker, About the influences of compressibility, heat transfer and pressure gradients in compressible turbulent boundary layers, *J. Fluid Mech.* **930**, A1 (2022).
- [43] D. Xu, J. Wang, and S. Chen, Skin-friction and heat-transfer decompositions in hypersonic transitional and turbulent boundary layers, *J. Fluid Mech.* **941**, A4 (2022).
- [44] H. Blasius, *Grenzschichten in Flüssigkeiten mit Kleiner Reibung* (Druck von BG Teubner, 1907).
- [45] N. Renard and S. Deck, A theoretical decomposition of mean skin friction generation into physical phenomena across the boundary layer, *J. Fluid Mech.* **790**, 339 (2016).
- [46] W. Li, Y. Fan, D. Modesti, and C. Cheng, Decomposition of the mean skin-friction drag in compressible turbulent channel flows, *J. Fluid Mech.* **875**, 101 (2019).
- [47] Y. Fan, W. Li, and S. Pirozzoli, Decomposition of the mean friction drag in zero-pressure-gradient turbulent boundary layers, *Phys. Fluids* **31**, 086105 (2019).
- [48] Q. Liu, Z. Luo, G. Tu, X. Deng, P. Cheng, and P. Zhang, Direct numerical simulations of a supersonic turbulent boundary layer subject to velocity-temperature coupled control, *Phys. Rev. Fluids* **6**, 044603 (2021).
- [49] D. Passiatore, L. Sciacovelli, P. Cinnella, and G. Pascazio, Finite-rate chemistry effects in turbulent hypersonic boundary layers: A direct numerical simulation study, *Phys. Rev. Fluids* **6**, 054604 (2021).
- [50] A. Elnahas and P. L. Johnson, On the enhancement of boundary layer skin friction by turbulence: An angular momentum approach, *J. Fluid Mech.* **940**, A36 (2022).

- [51] A. Kianfar, A. Elnahas, and P. L. Johnson, Quantifying how turbulent fluctuations enhance skin friction and surface heat transfer in boundary layers, in *AIAA SCITECH 2022 Forum* (AIAA, 2022), p. 0944.
- [52] A. Kianfar, M. Di Renzo, C. Williams, A. Elnahas, and P. Johnson, An angular momentum integral equation for high-speed boundary layers, in *Proceedings of the Summer Program, Center for Turbulence Research, Stanford University* (Stanford University, Stanford, California, 2022), pp. 357–366.
- [53] D. Xu, P. Ricco, and L. Duan, Decomposition of the skin-friction coefficient of compressible boundary layers, *Phys. Fluids* **35**, 035107 (2023).
- [54] M. Di Renzo and J. Urzay, Direct numerical simulation of a hypersonic transitional boundary layer at suborbital enthalpies, *J. Fluid Mech.* **912**, A29 (2021).
- [55] M. Di Renzo, L. Fu, and J. Urzay, HTR solver: An open-source exascale-oriented task-based multi-GPU high-order code for hypersonic aerothermodynamics, *Comput. Phys. Commun.* **255**, 107262 (2020).
- [56] S. Pirozzoli, Generalized conservative approximations of split convective derivative operators, *J. Comput. Phys.* **229**, 7180 (2010).
- [57] L. Fu, X. Y. Hu, and N. A. Adams, A family of high-order targeted ENO schemes for compressible-fluid simulations, *J. Comput. Phys.* **305**, 333 (2016).
- [58] S. Gottlieb, C.-W. Shu, and E. Tadmor, Strong stability-preserving high-order time discretization methods, *SIAM Rev.* **43**, 89 (2001).
- [59] R. K. Lobb, E. M. Winkler, and J. Persh, NOL hypersonic tunnel No. 4, results 7: Experimental Investigation of Turbulent Boundary Layers in Hypersonic Flow, Tech. Rep. (Naval Ordnance Lab, White Oak MD, 1955).
- [60] C. Williams, M. Di Renzo, P. Moin, and J. Urzay, Locally self-similar formulation for hypersonic laminar boundary layers in thermochemical nonequilibrium, Annual Research Briefs, Center for Turbulence Research, Stanford University (2021).
- [61] X. Wu, P. Moin, J. M. Wallace, J. Skarda, A. Lozano-Durán, and J.-P. Hickey, Transitional-turbulent spots and turbulent-turbulent spots in boundary layers, *Proc. Natl. Acad. Sci. USA* **114**, E5292 (2017).
- [62] F. M. White and G. H. Christoph, A simple theory for the two-dimensional compressible turbulent boundary layer, *J. Basic Eng.* **94**, 636 (1972).
- [63] R. D. Watson, Wall cooling effects on hypersonic transitional/turbulent boundary layers at high Reynolds numbers, *AIAA J.* **15**, 1455 (1977).
- [64] G. Araya, C. J. Lagares, J. Santiago, and K. E. Jansen, Wall temperature effect on hypersonic turbulent boundary layers via DNS, in *AIAA Scitech 2021 Forum* (AIAA, 2021), p. 1745.
- [65] S. Pirozzoli and M. Bernardini, Turbulence in supersonic boundary layers at moderate Reynolds number, *J. Fluid Mech.* **688**, 120 (2011).
- [66] D. Papamoschou and A. Roshko, The compressible turbulent shear layer: An experimental study, *J. Fluid Mech.* **197**, 453 (1988).
- [67] K. Matsuno and S. K. Lele, Internal regulation in compressible turbulent shear layers, *J. Fluid Mech.* **907**, R2 (2021).